

The ALPINE-ALMA [C II] survey. Dust attenuation curves at z = 4.4-5.5

Médéric Boquien, Véronique Buat, Denis Burgarella, Sandro Bardelli, Matthieu Béthermin, Andreas Faisst, Michele Ginolfi, Nimish Hathi, Gareth Jones, Anton Koekemoer, et al.

▶ **To cite this version:**

Médéric Boquien, Véronique Buat, Denis Burgarella, Sandro Bardelli, Matthieu Béthermin, et al.. The ALPINE-ALMA [C II] survey. Dust attenuation curves at z = 4.4-5.5. Astronomy and Astrophysics - A&A, 2022, 663, 10.1051/0004-6361/202142537 . insu-03780767

HAL Id: insu-03780767

https://insu.hal.science/insu-03780767

Submitted on 20 Sep 2022

HAL is a multi-disciplinary open access archive for the deposit and dissemination of scientific research documents, whether they are published or not. The documents may come from teaching and research institutions in France or abroad, or from public or private research centers.

L'archive ouverte pluridisciplinaire **HAL**, est destinée au dépôt et à la diffusion de documents scientifiques de niveau recherche, publiés ou non, émanant des établissements d'enseignement et de recherche français ou étrangers, des laboratoires publics ou privés.



Distributed under a Creative Commons Attribution 4.0 International License

A&A 663, A50 (2022)
https://doi.org/10.1051/0004-6361/202142537
© ESO 2022

Astronomy & Astrophysics

The ALPINE-ALMA [C II] survey. Dust attenuation curves at $z = 4.4–5.5$

Médéric Boquien[1], Véronique Buat[2,3], Denis Burgarella[2], Sandro Bardelli[4], Matthieu Béthermin[2], Andreas Faisst[5], Michele Ginolfi[6], Nimish Hathi[7], Gareth Jones[8,9], Anton Koekemoer[7], Brian Lemaux[10], Desika Narayanan[11,12], Michael Romano[13,14], Daniel Schaerer[15], Daniela Vergani[4], Giovanni Zamorani[4], and Elena Zucca[4]

[1] Centro de Astronomía (CITEVA), Universidad de Antofagasta, Avenida Angamos 601, Antofagasta, Chile
e-mail: mederic.boquien@uantof.cl
[2] Aix Marseille Univ., CNRS, LAM, Marseille, France
[3] Institut Universitaire de France (IUF), Paris, France
[4] INAF – Osservatorio di Astrofisica e Scienza dello Spazio di Bologna, via Gobetti 93/3, 40129 Bologna, Italy
[5] IPAC, California Institute of Technology, 1200 E California Boulevard, Pasadena, CA 91125, USA
[6] European Southern Observatory, Karl-Schwarzschild-Strasse 2, 85748 Garching, Germany
[7] Space Telescope Science Institute, 3700 San Martin Dr., Baltimore, MD 21218, USA
[8] Cavendish Laboratory, University of Cambridge, 19 J. J. Thomson Ave., Cambridge CB3 0HE, UK
[9] Kavli Institute for Cosmology, University of Cambridge,, Madingley Road, Cambridge CB3 0HA, UK
[10] Gemini Observatory, NSF's NOIRLab, 670 N. A'ohoku Place, Hilo, Hawai'i 96720, USA
[11] Department of Astronomy, University of Florida, 211 Bryant Space Science Center, Gainesville, FL 32611, USA
[12] Cosmic Dawn Center (DAWN), Niels Bohr Institute, University of Copenhagen, Juliane Maries vej 30, 2100 Copenhagen, Denmark
[13] Dipartimento di Fisica e Astronomia, Università di Padova, Vicolo dell'Osservatorio 3,35122 Padova, Italy
[14] INAF – Osservatorio Astronomico di Padova, Vicolo dell'Osservatorio 5, 35122 Padova, Italy
[15] Observatoire de Genéve, Université de Genéve, 51 Ch. des Maillettes, 1290 Versoix, Switzerland

Received 27 October 2021 / Accepted 21 February 2022

ABSTRACT

Context. There is ample evidence that dust is already present in abundance at high redshift. However, given the faintness of distant galaxies in the optical and the near-infrared, the data are limited and the understanding of how the dust affects the emerging radiation of galaxies at very high redshift is still limited.
Aims. Using the ALMA Large Program to INvestigate [C II] at Early times (ALPINE), our objective is to quantify the dust attenuation properties in galaxies at $z = 4.4–5.5$, particularly with regard to the shape of their attenuation curve.
Methods. Using the CIGALE spectral energy distribution (SED) code, we modeled the stellar populations and their interactions with the dust to measure some of the physical properties of the ALPINE sample. We selected a subsample of 23 main-sequence galaxies requiring a detection in at least six bands in the rest-frame UV and optical, as well as in the dust continuum around 158 µm or the [C II] fine-structure line. The inclusion of this line is important for improving the constraints on the physical properties, while achieving a reasonably low uncertainty on the slope of the attenuation curves.
Results. We find that the attenuation curves span a broad range of properties – from curves that are much steeper than the SMC extinction curve to those that are shallower than the starburst attenuation curve. The shape of the attenuation curves strongly depends on the V-band attenuation. Galaxies with the lowest attenuation also present the steepest curves. The steepness of such curves probably results from the combination of the intrinsic physical properties of the dust, the relative distribution of stars and dust in the interstellar medium, and the differential reddening, with an important fraction of the dust concentrated in star-forming regions. The broad range of attenuation curves found at $z \sim 5$ shows that no single attenuation curve is appropriate for main-sequence galaxies. When SED modeling is not feasible, assuming a fixed curve can lead to large errors, for instance, in the interpretation and application of the IRX-β diagram.
Conclusions. Considerable caution should be exercised when correcting high redshift galaxies for the presence of dust using the UV slope β as it can affect the estimation of both star formation rates and stellar mass even at low V-band attenuation due to the steepness of the attenuation curve. However, when SED modeling can be used, the impact of the choice of the attenuation curve on the star formation rate and the stellar mass is limited.

Key words. galaxies: high-redshift

1. Introduction

Dust is one of the key components of the interstellar medium (ISM) of galaxies. Not only does it dim and redden the far-ultraviolet (FUV) to near-infrared (NIR) radiation emerging from galaxies, which directly affects our ability to measure their physical properties, it also plays a key role in the matter cycle, acting as a catalyst in the formation of the molecular hydrogen that feeds star formation. While the formation of population III stars in a dust-free and metal-free context is not fully

understood, it is nevertheless clear that dust formed in large quantities early in the history of the universe (e.g., Riechers et al. 2013; Michałowski 2015; Watson et al. 2015; Burgarella et al. 2020; Péroux & Howk 2020).

In the absence of dust, the spectral emission of a normal star-forming galaxy is dominated by stellar populations of different ages with superimposed nebular emission, mainly in the form of recombination lines as well as continuum. The interaction with dust has a dramatic effect, both dimming and reddening the emission from stars and ionized gas. This negatively impacts our ability to measure star formation as energetic photons produced by massive young stars are far more easily attenuated than longer wavelength photons, and even a small quantity of dust can lead to a significant attenuation in the ultraviolet (UV). In the case of particularly dust-rich galaxies, it can render their detection in the rest-frame UV especially difficult. However, as the FUV emission vanishes due to dust attenuation, this dust re-emits the absorbed energy in the mid-infrared (MIR) and far-infrared (FIR), which can in turn be exploited to trace star formation. Except for the most extreme cases (e.g., when the dust content is negligible or, conversely, when almost all of the UV photons are absorbed by dust), an attenuation correction must be carried out to retrieve the star formation rate (SFR). One of the most direct ways is to simply apply a hybrid SFR estimator combining the rest-frame UV with the IR (e.g., Hao et al. 2011; Boquien et al. 2016). The obvious downside is that this requires observations of the dust emission that are costly and difficult to obtain, and even more so at increasing redshifts, where they tend to be limited to vanishingly small samples. With the rest-frame UV emission being relatively easy to obtain from the ground from $z \sim 2$ and beyond, techniques have been developed to relate the UV slope (β) to the UV attenuation (the IRX-β relation). While this approach initially appeared to work remarkably well in the case of starburst galaxies (Meurer et al. 1999), there is now ample evidence that there is no tight universal relation between the UV slope and the attenuation (e.g., Buat et al. 2005; Seibert et al. 2005; Howell et al. 2010; Casey et al. 2014). In fact, this relation relies on two strong underlying assumptions: the intrinsic UV slope of the stellar populations in the absence of dust and the exact shape of the attenuation curve. Numerous studies have analyzed their respective impact in an attempt to understand why and when such relations fail and build more reliable ones (e.g., Kong et al. 2004; Boquien et al. 2009, 2012; Popping et al. 2017, and many others). In particular, the recent study of Salim & Boquien (2019) found that the diversity of attenuation curves is a strong driver of the scatter around the IRX-β relation. This finding, which is consistent with simulations (Narayanan et al. 2018b; Liang et al. 2021), is especially important in that we can observe a broad variety of attenuation curves at all redshifts (e.g., Salmon et al. 2016; Buat et al. 2018; Salim et al. 2018). With the shape of the attenuation curve being strongly dependent on the relative geometry of stars, ionized gas, and dust (Salim & Narayanan 2020), from the disturbed morphologies observed at higher redshifts, we can only expect important variations there as well (e.g., Faisst et al. 2017). However, due to the great difficulty in measuring them and given the sparsity of the data available, our knowledge of attenuation curves beyond $z = 4$ remains limited. In effect, most observational studies on the attenuation properties of distant galaxies tend to concentrate on redshifts between 2 and 4 (e.g., Noll et al. 2009b; Buat et al. 2012, 2019; Reddy et al. 2012, 2015; Shivaei et al. 2015; Álvarez-Márquez et al. 2016; Salmon et al. 2016; Fudamoto et al. 2017, 2020b; Lo Faro et al. 2017; Álvarez-Márquez et al. 2019; Reddy et al. 2018; Koprowski et al. 2020). There is only a handful of examples at higher redshift (Capak et al. 2015; Scoville et al. 2015; Bouwens et al. 2016; Barisic et al. 2017; Koprowski et al. 2018). Because of the inherent limits of the observations, studies based on numerical simulations of galaxies at very high redshift (e.g., Mancini et al. 2016; Cullen et al. 2017; Di Mascia et al. 2021) are an important source of information. However, they lead to contrasted results, finding both flat (Cullen et al. 2017) and steep (Mancini et al. 2016) attenuation curves.

With the rapid build-up of dust at high redshift and the range of new facilities that will come online through the 2020s to peer into distant galaxies with unprecedented detail, it is a timely undertaking to shed a new light on dust attenuation in the early universe. To reach this goal, we exploit the ALPINE (ALMA Large Program to INvestigate [C II] at Early times, Le Fèvre et al. 2020) survey, along with ancillary multi-wavelength data in combination with the CIGALE spectral energy distribution (SED) modeling code (Burgarella et al. 2005; Noll et al. 2009a; Boquien et al. 2019).

The article is organized as follows. We briefly present ALPINE and the sample selection in Sect. 2. We describe our SED modeling to measure the physical properties of the galaxies in our sample in Sect. 3. We present the results in Sect. 4, along with a discussion in Sect. 5 and our conclusion in Sect. 6. Throughout this article, we assume a Chabrier (2003) initial mass function (IMF) and a flat Λ cold dark matter cosmology, with $H_0 = 70\,\mathrm{km\,s^{-1}}$, $\Omega_m = 0.3$, and $\Omega_\Lambda = 0.7$.

2. Sample

2.1. ALPINE survey

ALPINE is a large survey of 118 high-redshift ($4.4 \lesssim z \lesssim 5.9$) galaxies observed with ALMA (Le Fèvre et al. 2020), targeting the [C II] line at 158 µm. In a nutshell, the ALPINE sample in based on the COSMOS (Scoville et al. 2007) and ECDFS (Giacconi et al. 2002) surveys. Its galaxies were selected from the UV ($L_{\mathrm{UV}} > 0.6L^*$) and sources hosting a type I active galactic nucleus were specifically excluded. Finally, to ensure proper targeting of the [C II] line with ALMA, all the objects had to have a secure redshift. The resulting sample is representative of star-forming galaxies down to an SFR of $1\,M_\odot\,\mathrm{yr}^{-1}$ around a redshift of 5. As we show in Sect. 4.1.1, our ALPINE subsample follows the main sequence at that redshift closely. The survey and the complementary data have been described in great detail in Le Fèvre et al. (2020), Béthermin et al. (2020) and Faisst et al. (2020) and we refer to these articles for more information on the sample, the observations, and data processing.

Being the largest targeted survey of high-redshift galaxies with ALMA, it is clear that ALPINE is a real treasure trove for the study of outflows (Ginolfi et al. 2020), mergers, and morpho-kinematic diversity (Le Fèvre et al. 2020; Jones et al. 2020, 2021; Romano et al. 2021), as well as Ly-α emitters (Cassata et al. 2020), [C II] as an SFR tracer (Schaerer et al. 2020), [C II] sizes (Fujimoto et al. 2020), molecular gas (Dessauges-Zavadsky et al. 2020), [C II] luminosity functions (Yan et al. 2020; Gruppioni et al. 2020; Loiacono et al. 2021), the main sequence (Khusanova et al. 2021), and the dust mass budget (Pozzi et al. 2021), and even the study of serendipitously discovered objects (Gruppioni et al. 2020; Romano et al. 2020; Loiacono et al. 2021). Of particular interest to the current paper is the study of Fudamoto et al. (2020a), who delved into the attenuation properties of ALPINE galaxies. In a nutshell,

these authors examined the relation between IRX, the stellar mass ($M_\star$), and β. They found that, via a stacking analysis and for the galaxies detected in the dust continuum, the attenuation curve is steeper than for galaxies at lower redshift, but with an smaller attenuation overall. This study focused on the exploitation of rest-frame UV-optical data modeled with the LePhare code (Arnouts et al. 1999; Ilbert et al. 2006) on the one side and ALMA observations on the other – independently from one another. However, given the high quality of the ALPINE data, an alternative approach is to model the full multi-wavelength emission simultaneously with the ALMA observations. This allows for more reliable estimates to be obtained, related to the physical properties of galaxies, albeit on a smaller scale. We present this approach in greater detail in Sect. 3.

2.2. Available data and sample selection

For this work, in addition to the ALMA data, we consider all the bands presented in Faisst et al. (2020), ranging from ∼360 nm to 8 µm in the observed frame. However, as described in Sect. 3.2, requirements on a minimum signal-to-noise ratio (S/N) means that for each object, only a fraction of the available bands are used in the fits.

We divided the data into two tiers, to which further cuts are applied (see Sects. 3.2 and 3.3). Tier 1 is initially comprised of the 21 galaxies that have been detected both in the continuum around 158 µm rest-frame and in the [C II] line. Tier 2 is made of the 53 galaxies that are not detected in the continuum but their [C II] emission is. We excluded a total of 43 galaxies from our final sample. Two of them are detected in the dust continuum around 158 µm but not in the [C II] line. This deficit can be suggestive of the presence of an obscured active nucleus (e.g., Sargsyan et al. 2012, 2014) that would negatively affect the reliability of our measurements. In addition, the uncertainty on the spectroscopic redshift of these two objects is such that the [C II] line may have fallen outside the ALMA spectral window. The other 41 objects are detected neither in [C II] nor in the continuum and are deemed too unreliable for this analysis as the lack of FIR detection severely hampers our ability to constrain many of the physical properties that are critical for constraining the attenuation curves, as we show in Sect. 3.4. We find that many of these objects are very blue and, along with the fact of their non-detection by ALMA, this suggests that they are very dust-poor. Others unfortunately lack data at short wavelengths, which limits the constraints on their UV properties. However, this does suggest that most of these objects have a low mass, making them too faint to be detected at a sufficient level in the UV-optical.

3. Multi-wavelength modeling

3.1. CIGALE

To measure the physical properties of the sample, we carried out a multi-wavelength modeling process with CIGALE (Burgarella et al. 2005; Noll et al. 2009a; Boquien et al. 2019). In brief, CIGALE is an energy balance SED modeling code that includes flexible star formation histories, stellar populations, and dust in absorption and emission, and it relies on Bayesian inference to estimate the physical properties of galaxies. The idea behind energy balance is that the luminosity absorbed by the dust in the UV-to-NIR is re-emitted self-consistently in the MIR and FIR. Modeling and fitting the full SED simultaneously is particularly useful for breaking degeneracies. For instance, a galaxy can be optically red either because it is very dusty or because it does not contain young stellar populations. In the former case, the dust emission will be higher than in the latter. The energy balance allows us to determine the actual nature of the object. At the same time, the Bayesian inference technique is essential to estimate reliably the physical properties.

Another key feature is that CIGALE seamlessly handles upper limits, which allows us to obtain constraints in the case of non-detections. It is based on the method presented in Sawicki (2012). We refer in particular to Sect. 4.3 of Boquien et al. (2019) for its implementation in CIGALE. The handling of upper limits is especially important for this work as the dust continuum is undetected in over two-thirds of the sample. At the same time, CIGALE can also fit physical properties that are intensive (i.e., independent from the size of the object such as the age) and extensive (dependent on the size of the object such as the luminosity), rather than just the fluxes. We used these features to exploit both the dust continuum and the [C II] line ALMA observations. For the 21 galaxies for which the 158 µm continuum emission was measured, the dust luminosity is a strong constraint on energy balance and we fit this extensive property along with the panchromatic fluxes. Rather than estimating the dust luminosity ourselves, we adopted the meticulously derived values of Béthermin et al. (2020), who used a combination of models with empirical fits. For tier 2 galaxies, only [C II] is detected. This is not a quantity that can be computed in CIGALE models. Indeed, given the important variations in the luminosity of this fine-structure line which are not well-understood, modeling reliably the [C II] emission of galaxies is especially difficult. We therefore fit the SFR after a conversion from [C II], which provides us with a more indirect and less reliable constraint on the energy balance compared to the dust luminosity. For this, we use the carefully curated statistical relation between the [C II] luminosity and the total SED-based SFR (obscured and unobscured) presented in Schaerer et al. (2020), $\log(L([\mathrm{C\,II}])/L_\odot) = 7.05 + 0.96 \times \log(\mathrm{SFR}/M_\odot\,\mathrm{yr}^{-1})$, which is based on models with LePhare. In addition to the SFR and the multi-wavelength fluxes, we also include upper limits on the dust luminosity in the fit.

We use the following strategy to model our sample of galaxies. First, we assumed a delayed star formation history (SFH): $\mathrm{SFR} \propto t \times \exp(-t/\tau)$, with t the time elapsed since the beginning of star formation and τ the time at which the SFR reaches its maximum value. Assuming that the first star was born approximately 100 Myr after the big bang, we fixed t to 900 Myr for galaxies at $z \sim 5.5$ and 1300 Myr for galaxies at $z \sim 4.5$. Based on a simple physical argument, this allows fixing a parameter that is otherwise poorly constrained, which can have negative effects on the determination of other physical properties. We allow τ to vary from 100 Myr (star formation peaks early) to 1300 Myr (the SFR always increases over the timespan considered) in steps of 200 Myr. In practice the assumption of an inflexible functional form, such as that of a pure delayed SFH, can bias the measure of some key physical properties of galaxies (Ciesla et al. 2017; Lower et al. 2020) and lead to overly rigid relations between SFR and $M_\star$ with little dispersion. To solve this, we add a second component to take into account the most recent episode of star formation. For simplicity, we assume that this episode can be modeled as a constant SFR over a duration of 10, 25, 50, 75, or 100 Myr and whose strength is parametrized by the fraction of the stellar mass formed during this episode, with respect to the total stellar mass formed over the lifetime of the galaxy. We sampled the mass fraction with 21 linearly spaced values from 0% (no burst) to 10% (strong burst). One characteristic to note is that at high redshift, it has been argued that

that the SFR should be rising on average, as indicated by the cosmic SFR density evolution (Madau & Dickinson 2014). With the adopted parametrization, this is possible through two mechanisms. First, when τ is larger than the age, the SFR is always increasing over the considered period. Then, there is a possibility for a fairly strong episode of star formation, even when there is a decrease in the SFR on the middle term. Overall, this parametrization allows us to have a variety of SFH, which yields a dispersion of ±0.3 dex around the main sequence as we show in Sect. 4.1.1. A consequence of the flexibility is that the uncertainties on the physical properties are larger but probably more realistic. This is due to degeneracies that are otherwise not taken into account with smooth and rigid SFH. For instance, the spectrum of a galaxy with a stronger but older episode of star formation will be fairly similar to that of a galaxy with a weaker but more recent episode of star formation.

With the SFH defined, we computed the stellar spectrum using the Bruzual & Charlot (2003) single stellar populations, assuming a Chabrier (2003) IMF, and a metallicity of $Z = 0.008$, as a compromise between metallicities of $Z = 0.02$ (solar) and $Z = 0.004$ adopted by Faisst et al. (2020). This choice is motivated by the fact that the galaxies in our subsample are reasonably massive for this redshift ($M_\star \gtrsim 10^{10}\,M_\odot$) and at such masses, Faisst et al. (2016) found $12 + \log \mathrm{O/H} = 8.32^{+0.40}_{-0.74}$ for galaxies at $z \sim 5$. Given the range of masses reaching over $10^{11}\,M_\odot$ and that there is an important dispersion making it difficult to assign a specific metallicity to a given galaxy, a subsolar metallicity of $Z = 0.008$ appears reasonable. This being said, the choice of the metallicity only has a very small influence on the estimates of the attenuation curve and it does not affect our conclusions. We then add a nebular component that includes the continuum (free-free, free-bound, and 2-photon processes) as well as hydrogen and metal recombination lines, which are scaled based on the production rate of Lyman continuum photons. This is important because at high redshift, the equivalent width of emission lines can become very large and thus account for a substantial fraction of the total flux in passbands (e.g., Sargent & Searle 1970; Atek et al. 2011; Yuan et al. 2019). We adopted an ionization parameter $\log U = -2$ but adopting a lower value of $\log U = -3$ gives qualitatively identical results. The next step concerns the attenuation. As mentioned earlier, there is now established evidence of ample variations in the attenuation curves of galaxies. To account for this, we have chosen a bump-free modified Calzetti et al. (1994, 2000) prescription (Noll et al. 2009a, see Sect. 4.2 for the specific motivation for this choice). In short, it considers a starburst curve extended by the Leitherer et al. (2002) curve under 180 nm. The resulting curve is then modified by multiplying it with a power law with a free index δ ($\propto \lambda^\delta$) ranging from −2.0 (steeper) to 0.5 (shallower) and that is applied both on the stellar and the gas emission without differential reddening so that the effective attenuation curve is directly tied to δ. For clarity, $\delta = 0$ corresponds to a bona fide starburst attenuation curve and is also similar to a Milky Way extinction curve in the optical, $\delta = -0.3$ is akin to a Large Magellanic Cloud extinction curve (avoiding the bump), and $\delta = -0.5$ to a Small Magellanic Cloud extinction curve. We show these curves in Fig. 1. Even though curves steeper than that of the Small Magellanic Cloud may seem unusual, they can be found both in simulations (e.g., Trayford et al. 2020) and observationally (e.g., Salim et al. 2018). Finally, we included the intergalactic medium (IGM) of Meiksin (2006), which has a strong effect at these redshifts on the radiation shortward of Ly-α, and we redshifted the spectra. We would like to emphasize that even though this set of models has been optimized for the measurement of attenuation properties, we ensured that the SFH is flexible enough to cover variations we could expect from main sequence galaxies. Additional analyses using models with either lower or higher degrees of flexibility in their SFH have shown that they ultimately lead to qualitatively similar results.

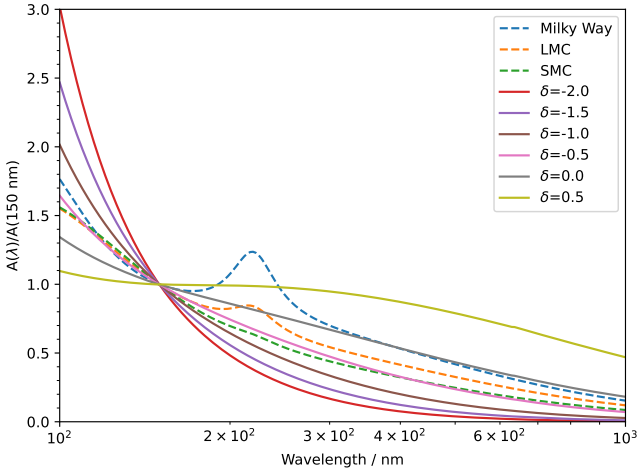


Fig. 1. Modified starburst attenuation curves normalized to 150 nm for different values of δ (solid lines). A starburst curve corresponds to $\delta = 0$. The models include 101 curves ranging from $\delta = -2$ to $\delta = 0.5$. For comparison, we also plot the extinction curves of the Milky Way, the Large Magellanic Cloud, and the Small Magellanic Cloud (dashed lines).

Sampling this parameter space, we fit 14 847 000 models to each galaxy. For the entire sample, we computed and fit (including to a synthetic catalog, see Sect. 3.4) a total of 727 503 000 models to all the galaxies in approximately 15 h on a 48-core dual AMD EPYC 7451 server. We give the modules and their corresponding parameters in Table 1.

Finally, the physical properties and their uncertainties are estimated by computing the likelihood-weighted mean and standard deviation of the parameters of all the models fitted to the data. The attenuations are determined for each model computing the dust-free and dust-attenuated luminosities through the GALEX FUV and the Bessel V bands. The IRX parameter is taken as the decimal logarithm of the dust luminosity to the restframe UV luminosity in the GALEX FUV filter. The UV slope β is computed by fitting a powerlaw on the restframe UV spectrum of each model using the wavelength windows defined in Calzetti et al. (1994). The dust-free UV slope β_0 is computed in the same way. All the other parameters either correspond to input parameters (δ) or to values derived from the models (SFR and $M_\star$).

3.2. Band selection and adjustment of uncertainties

We constructed the photometric table using the compilation of Faisst et al. (2020) in the rest-frame UV-optical, which is based on the COSMOS15 (Laigle et al. 2016) and 3D-HST (Brammer et al. 2012; Skelton et al. 2014) catalogs; these, in turn, were based on the HST imaging obtained by CANDELS (Grogin et al. 2011; Koekemoer et al. 2011). From this large dataset, we eliminate bands contaminated by the Ly-α line due to its uncertain escape fraction. We also remove bands at shorter wavelengths as the intervening IGM renders the models somewhat less reliable in this range and because there is evidence that the attenuation curve flattens at shorter wavelengths at low

Table 1. Modules and their corresponding parameters used by CIGALE for building a grid of 727 503 000 models (14 847 000 models at a given redshift) and estimate the physical properties of the ALPINE sample.

Module	Parameter	Value
sfhdelayed	age_main (Myr)	900 ($z \sim 5.5$) or 1300 ($z \sim 4.5$)
	tau_main (Myr)	100, 300, 500, 700, 900, 1100, 1300
	age_burst (Myr)	10, 25, 50, 75, 100
	tau_burst (Myr)	1e10
	f_burst	21 linearly spaced values from 0.0 to 0.1
bc03	imf	1 (Chabrier 2003)
	metallicity ($Z_\odot$)	0.008
nebular	logU	-2
	f_esc	0
	f_dust	0
	lines_width (km s^{-1})	300
dustatt_calzleit	E_BVs_young	100 linearly spaced values from 0.005 to 0.500 mag
	E_BVs_old_factor	1.0
	powerlaw_slope	101 linearly spaced values from -2.0 to 0.5
	filters	FUV, V_B90, 150, 550
restframe_parameters	beta_calz94	true
	D4000	false
	IRX	true
	EW_lines	—
	luminosity_filters	—
	colours_filters	—
redshifting	redshift	—

Notes. We refer to Appendix C of Boquien et al. (2019) for a detailed definition of each parameter.

redshift (Buat et al. 2002; Leitherer et al. 2002) as well as for more distant galaxies (Reddy et al. 2016), which would only add to the uncertainties.

An important aspect to note is that in order to avoid overfitting due to underestimated flux uncertainties, we followed the strategy of Faisst et al. (2020) that was adopted for the LePhare modeling. We scaled the uncertainties upward by 10% and we added in quadrature 0.01 mag for ground-based images, 0.05 mag for intermediate bands, 0.1 mag for *Spitzer* 3.6 µm and 4.5 µm, and 0.3 mag for *Spitzer* 5.8 µm and 8.0 µm. At the same time, we disabled the additional uncertainty of 10% that is included in CIGALE by default.

To prevent diluting the fit with a large number of low-quality fluxes, we made a further band down selection object by object, selecting only bands detected at a S/N of at least 3. We limit the selection to objects with a least six non-ALMA observations so that a sufficient number of bands is available to constrain the attenuation curve. This reduces the sample to 20 tier 1 and 32 tier 2 galaxies.

Overall we included: the Subaru/Suprime-Cam (i', z', and z'', IA709, IA738, IA767, IA827, IA856, NB711, and NB816), Subaru/Hyper-Suprime-Cam (y), *Spitzer* IRAC (3.6 µm, 4.5 µm, 5.8 µm, and 8.0 µm), CFHT/WIRCAM (H^w and K_s^w), CFHT/VIRCAM (Y, J, H, and K_s), HST/ACS (F755W and F814W), HST/WFC3 (F125W, F140W, and F160W), MPG-ESO/WFI (I), and VLT/ISAAC (J, H, and K_s) bands.

3.3. Final sample selection

Finally, we only considered galaxies with a maximum absolute uncertainty on the slope δ of 0.45. The reason for doing so is that the inclusion of galaxies with poor constraints on δ may affect our conclusions. The choice of this value is somewhat subjective. However, an uncertainty of 0.45 on δ keeps the estimated uncertainty well under a quarter of the full range. Naturally, this criterion tends to exclude galaxies that are not detected in the dust continuum and, by extension, galaxies at low attenuation with a flat attenuation curve (see Sect. 5.3). This being said, we find that this choice is appropriate to discriminate with confidence between different regimes of attenuation curves.

Unsurprisingly, this final selection criterion has a strong effect on the tier 2 sample in particular, which is reduced to 9 galaxies. The reason is that only having upper limits on the dust continuum emission limits our ability to constrain the shape of the attenuation curve. The final tier 1 sample suffers from a much more modest reduction in its size, down to 14 galaxies. Out of the 23 galaxies of our final sample, 4 are located beyond a redshift of 5.

As an illustration, we show examples of typical fits of tier 1 galaxies in Fig. 2. The complete set of best-fits is presented in Figs. A.1 and A.2 for the rest of tier 1 and tier 2 galaxies. The physical properties (IRX, β, δ, AFUV, A_V, SFR, and $M_\star$) and the corresponding uncertainties for these 23 galaxies are presented in Table B.1. For clarity, all these physical properties are directly estimated from CIGALE. IRX is computed as the ratio of the total dust luminosity to the luminosity in the GALEX FUV band and β is determined by fitting the UV continuum in the spectral windows given in Table 2 of Calzetti et al. (1994).

3.4. Reliability of the estimation of physical properties

One important improvement over the modeling presented in Faisst et al. (2020), Fudamoto et al. (2020a) is the inclusion of ALMA observations (both the [C II] line and the total infrared luminosity). First, the ALMA data may bring decisive information to break degeneracies, for instance, between the SFH and

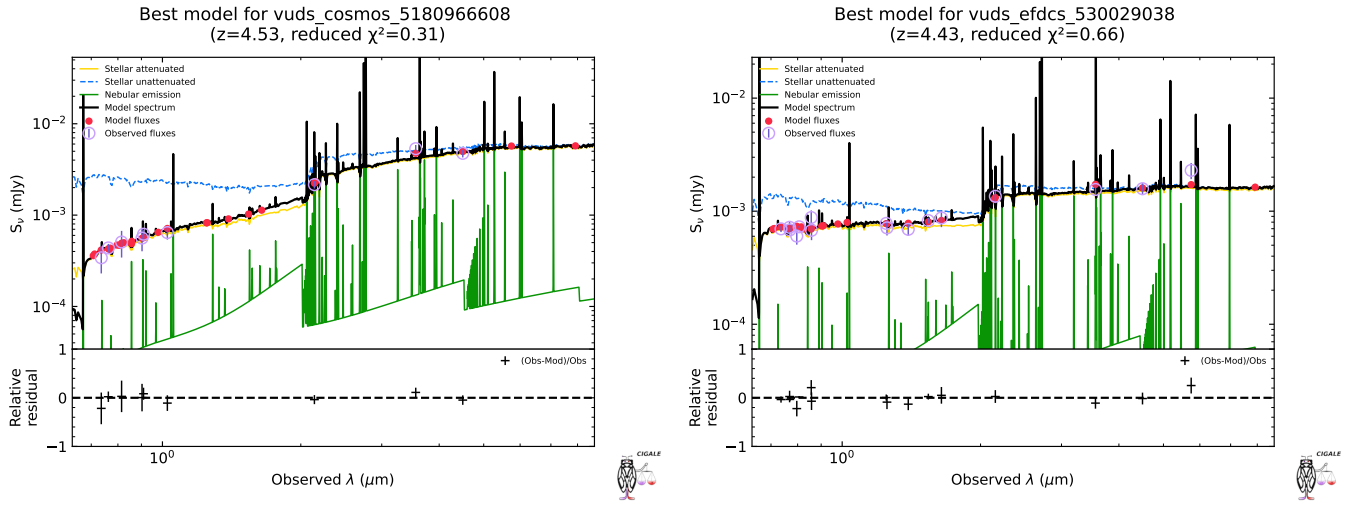


Fig. 2. Best fits of galaxies vuds_cosmos_5180966608 at $z = 4.53$ (*left*) and vuds_efdcs_530029038 at $z = 4.43$ (*right*). The galaxy spectra are shown in black, with the dust-attenuated stellar populations in yellow and the ionized gas in green. For comparison, the dust-free stellar populations are shown in blue. The model fluxes integrated in passbands are shown as red circles and the observations and 1-σ uncertainties are indicated with purple circles with vertical lines. Finally, the relative residuals are shown in the *bottom panels* of each plot.

the attenuation. In order to assess the capacity of the modeling to reliably estimate the physical properties with and without ALMA data, we follow the strategy of Giovannoli et al. (2011). We first build a synthetic catalog from the best-fits. For each object, random perturbations are then injected into the best-fit fluxes. These perturbations are drawn from a Gaussian distribution with a standard deviation corresponding to the uncertainty given in the input catalog. Finally, we fit this synthetic catalog and we compare the Bayesian estimates of the physical properties to the exact values obtained from the original best-fits. We show the results in Fig. 3. It appears that AFUV, δ, β, IRX, SFR, and $M_\star$ are all well determined for objects from tiers 1 and 2.

If we fit the same objects, this time not including the ALMA observations, we obtain a starkly different picture as demonstrated by the strongly increased standard deviation for most physical properties. The estimates for these physical properties appear much more uncertain. This is true in particular for δ, which is left nearly unconstrained, with little dependence between the true and estimated values, especially for the steepest slopes. For other physical properties, the scatter is visibly larger in most cases. This is notably the case of AFUV, IRX, and the SFR. This demonstrates once again the importance of observing the emission of the dust and [C II] (taken indirectly into account through the SFR) in order to constrain the physical properties of galaxies.

We must emphasize that using synthetic catalogs, our main aim here is to verify that with the current set of observations and models, the code is able to retrieve the physical properties self-consistently. For the physical properties it cannot retrieve, then we have the assurance that we cannot trust these estimates. For the physical properties that are well-retrieved, we can trust these estimates to the extent that the choice of the models is appropriate. So, even though such tests are not foolproof they are efficient at uncovering limitations in the estimation of the physical properties.

4. Results

4.1. General properties: SFR, $M_\star$, IRX, and β

As mentioned earlier, Fudamoto et al. (2020a) explored the relation between IRX, $M_\star$, and β in the ALPINE sample. The major difference in our case is that we compute all the physical properties of each galaxy through self-consistent SED modeling from rest-frame FUV to 158 μm. Here, we examine the relations between these quantities, also including the SFR.

4.1.1. SFR-$M_\star$ relation

As the SFR and $M_\star$ are tightly related, the latter being directly dependent on the integral of the former, the scaling relation between these two quantities is one of our main tools to understand the evolution of galaxies across redshifts (e.g., Brinchmann et al. 2004; Noeske et al. 2007 and many others). It is found that most massive galaxies form more stars but in a somewhat sublinear fashion and that at fixed mass, galaxies at lower redshift tend to form stars at a lower rate. We examine in Fig. 4 the relation between SFR and $M_\star$ followed by our sample. We see that it forms a well-defined sequence over approximately a dex in both SFR and $M_\star$ and matches the relation inferred by Speagle et al. (2014). This is expected as the original ALPINE sample was constructed to contain normal star-forming galaxies and we observe a good agreement with the stacks of Khusanova et al. (2021).

A fair question, however, would consider how the SFR compares with that obtained from simple estimators that are often used at high redshift. To answer this question, we have converted the rest-frame FUV emission estimated with CIGALE and the dust luminosity to SFR using the conversion factors presented in Kennicutt & Evans (2012). After conversion to the Chabrier (2003) IMF using the coefficients of Madau & Dickinson (2014), we find that the sum of the FUV and dust SFR show no offset compared to the SFR determined with CIGALE with the average logarithmic difference equal to 0.00 ± 0.05 dex.

4.1.2. IRX-β relation

As we have described in Sect. 1, the relation between IRX and β is an important tool to quantify the attenuation of galaxies. However, it is now well established that there can be important deviations away from the original relation (Meurer et al. 1999), which was derived for UV-bright starburst galaxies. Three physical

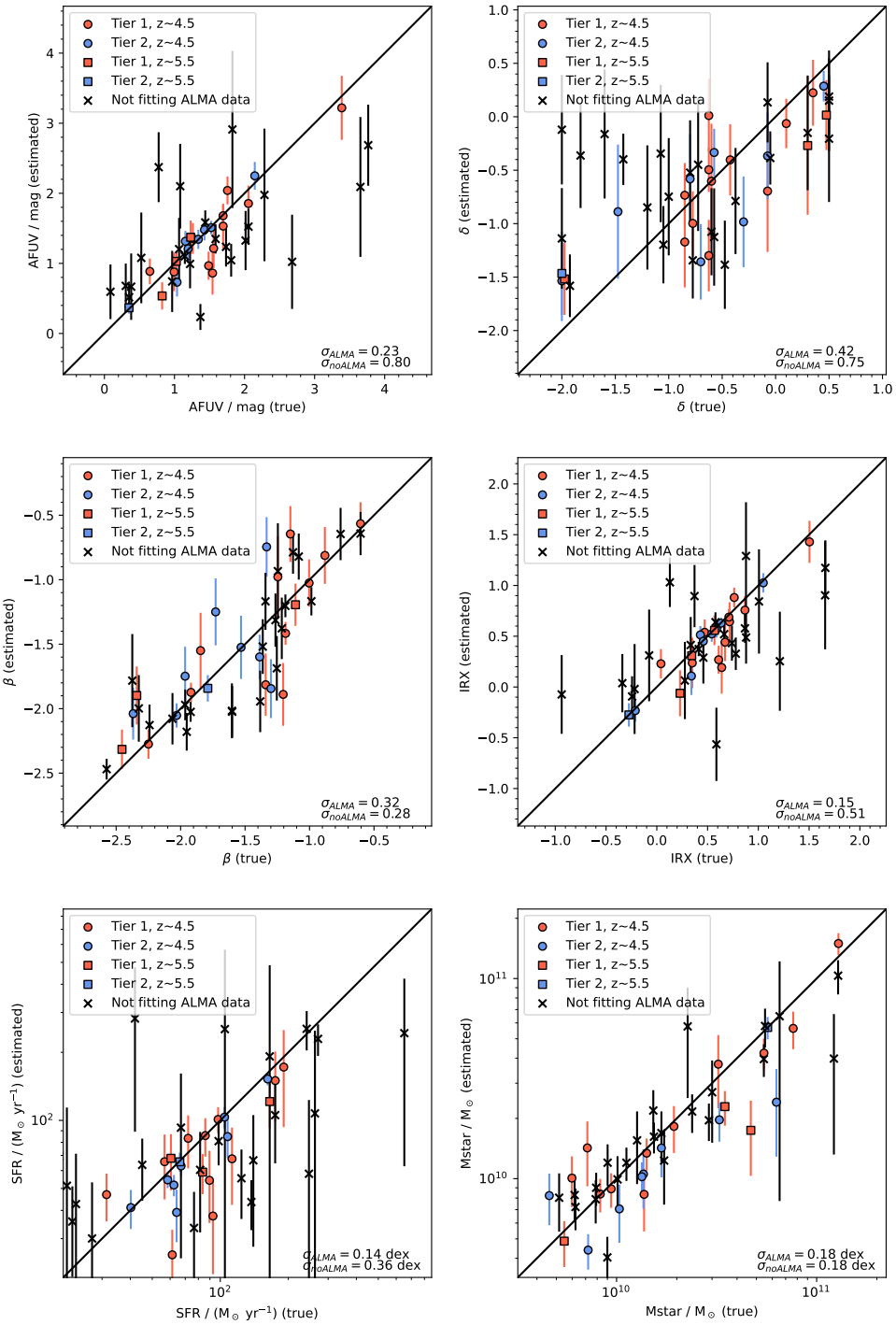


Fig. 3. Comparison of the true (x axis) and estimated values (y axis) for AFUV, δ, β, IRX, SFR, and $M_\star$, *from top-left to bottom-right*. The solid black line indicates the one-to-one relation. The red (blue) symbols represent galaxies detected in the continuum at 158 µm rest-frame (detected only in the [C II] line). The black crosses represent the same objects when the ALMA data ([C II] and/or 158 µm continuum) are not taken into account in the fit, essentially limiting it to rest-frame UV and optical observations. The inclusion of ALMA data visibly improves the estimates of many of the physical properties. For a physical property as difficult to estimate as the slope of the attenuation curve δ, the inclusion of ALMA data is decisive. Even though the scatter remains important, in particular for the steepest (most negative δ) curves, this is a considerable progress compared to the situation without ALMA observations for which constraints are much more lax. The standard deviation of the physical properties estimated with and without ALMA data is indicated in the *bottom-right corner* of each panel.

properties play a key role in defining the locus of a galaxy in the IRX-β plane: the intrinsic UV slope β_0 in the absence of dust, which depends on the SFH as well as on the intrinsic properties of the stellar populations, and the shape and the amplitude of the attenuation curve, which has the effect of reddening the stellar spectrum. The more dust, the redder the UV slope β is at fixed attenuation curve slope. Similarly, the steeper the slope of the attenuation curve, the redder the UV slope β is at fixed amplitude of the attenuation. At the same time, a redder β_0 will also yield a redder β. In the end, interpreting IRX-β diagrams to

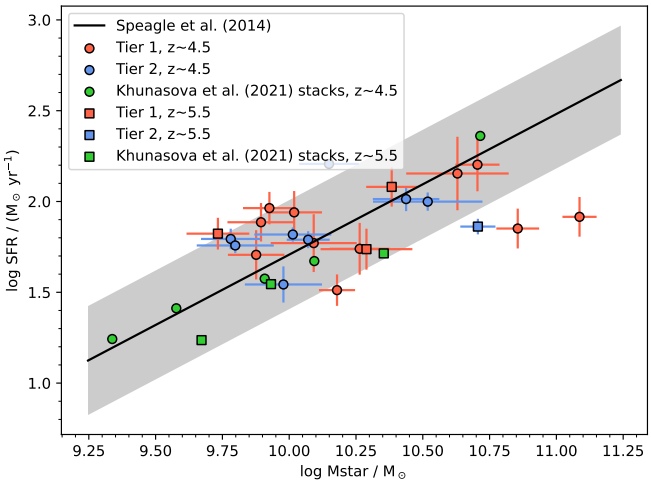


Fig. 4. Relation between the SFR and $M_\star$ as estimated by CIGALE for our sample. The symbols are identical to those of Fig. 3, with the addition of the stacks of Khusanova et al. (2021) in green. The black line corresponds to the relation derived by Speagle et al. (2014) at $z \sim 5$, converted from a Kroupa (2001) to a Chabrier (2003) IMF. The shaded area corresponds to a typical ±0.3 dex scatter in SFR. We see that it forms a well-defined sequence over approximately a dex in both SFR and $M\star$ and matches the relation inferred by Speagle et al. (2014). This is expected as the original ALPINE sample was constructed to contain normal star-forming galaxies.

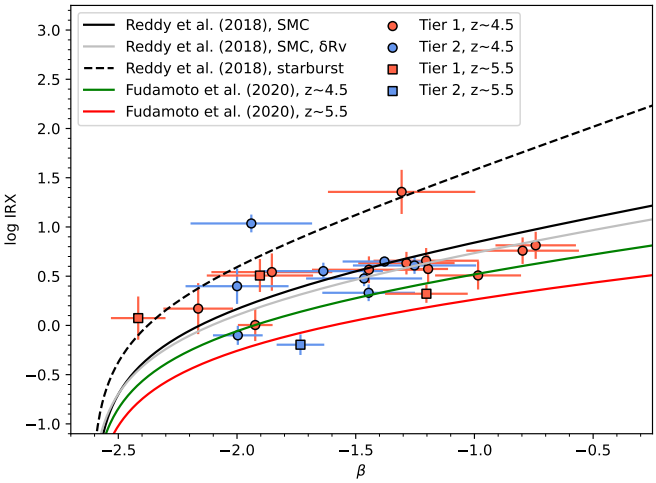


Fig. 5. Relation between IRX and β as estimated by CIGALE in our sample. The symbols are identical to those of Fig. 3. The lines correspond to different previously published relations. The dashed black, solid black and gray lines respectively correspond to the starburst, unmodified SMC, and SMC with a modified Rv attenuation curves, as published in Reddy et al. (2018). The green and red lines correspond to relations derived by Fudamoto et al. (2020a) for stacked ALPINE galaxies at $z \sim 4.5$ and $z \sim 5.5$, respectively. The reasonably small range in the intrinsic UV slope β_0 and the distribution of the data with respect to various relations suggest that the dispersion is driven by variations of the attenuation curves across the sample.

estimate the attenuation always bears the uncertainty of an incorrect assumption on these parameters.

In Fig. 5, we plot the IRX-β relation for the galaxies in our sample. We see that the sample covers the full range, from attenuation curves shallower than the starburst attenuation curve, to steeper than the SMC extinction curve. The relations of Fudamoto et al. (2020a) computed from ALPINE stacks at $z \sim 4.5$ and $z \sim 5.5$ form an approximate lower limit for our sample.

As mentioned above, the assumption on β_0 can affect the interpretation of this diagram. Both Reddy et al. (2018) and Fudamoto et al. (2020a) assume $\beta_0 = -2.62$, which is bluer than classical relations probably from differences in the stellar models as Reddy et al. (2018) used the BPASS models (Eldridge & Stanway 2009), which include a refined treatment of binary evolution. For comparison, Meurer et al. (1999) assume $\beta_0 = -2.23$. In addition, adopting a fixed β_0, there is the implicit assumption that all galaxies have the same intrinsic color. To assess whether setting $\beta_0 = -2.62$ is sound, we examine the CIGALE estimates of β_0. We find that over our final sample of 23 galaxies, $\langle\beta_0\rangle = -2.54 \pm 0.07$. Even though it is slightly redder than the adopted value of Reddy et al. (2018), the difference remains small. Another possible point of comparison is with numerical simulations. Mancini et al. (2016) find $\langle\beta_0\rangle \lesssim -2.5$ for galaxies at $z = 5-8$. For synthetic objects at $z \sim 5$, Cullen et al. (2017) find $\langle\beta_0\rangle = -2.52$. Interestingly, these values appear consistent even though these studies lead to very different attenuation curves. Overall, this shows that, at least from the point of view of UV colors, our stellar populations are consistent with both observations and simulations. In contrast, adopting the starburst relation of Reddy et al. (2018), to reproduce the observations β_0 would need to range from −3.0 to −1.5. Such a broad range seems unlikely given the selection of the sample and the previous considerations. By extension, this means that the dispersion we find is probably driven by variations of the attenuation curve across our sample. Indeed, we find that even though a few points are compatible with the starburst relation, this is excluded for a substantial part of the sample beyond the 3-σ level. Conversely, many points are compatible with the SMC curve at 2-σ, with just a few galaxies beyond 3-σ. We examine the variations of the attenuation curve in more detail in Sect. 4.2.

4.1.3. IRX-$M_\star$ relation

Measuring the slope β can be challenging and uncertain for distant galaxies, at least relative to the measure of the stellar mass. Consequently, there has been a number of studies establishing a relation between IRX and $M_\star$ as an alternate way to estimate the dust attenuation in galaxies (e.g., Xu et al. 2007; Buat et al. 2009; Heinis et al. 2014; Bouwens et al. 2016; Bogdanoska & Burgarella 2020; Fudamoto et al. 2020b). In their study of ALPINE galaxies, Fudamoto et al. (2020a) found that there is an evolution of the normalization of the relation with redshift. This is to be noted as, at lower redshifts, the relation shows little change. This was shown at $z \sim 2-3$ by Bouwens et al. (2016) who compiled the relations of Reddy et al. (2010), Whitaker et al. (2014), Álvarez-Márquez et al. (2016). We show in Fig. 6 the relation between IRX and $M_\star$, which has been determined using CIGALE while taking into account constraints from ALMA observations. Similarly to Fudamoto et al. (2020a), we find that our sample of ALPINE galaxies also follows the relation of Fudamoto et al. (2020b), which was computed using an unbiased sample, while falling clearly below the relation of Bouwens et al. (2016). The small number of $z \sim 5.5$ galaxies is not sufficient to comment in detail on an evolution from $z \sim 4.5$. However, in their study which included stacks, Fudamoto et al. (2020a) noted a further decrease in the normalization at higher redshift. Overall, we find that the addition of ALMA constraints and the

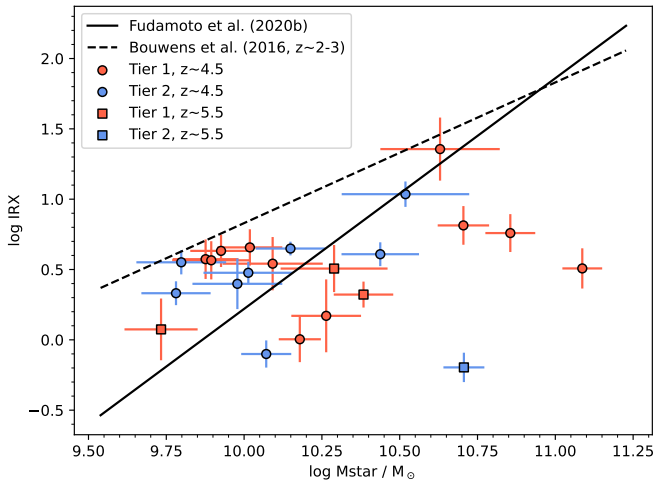


Fig. 6. Relation between IRX and $M_\star$ as estimated by CIGALE in our sample. The symbols are identical to those of Fig. 3. The solid and dashed lines correspond to the relations of Fudamoto et al. (2020b) at $z \sim 3$ and the relation of Bouwens et al. (2016), respectively. Similarly to Fudamoto et al. (2020a), we find that our sample of ALPINE galaxies also follows the relation of Fudamoto et al. (2020b), which was computed using an unbiased sample, while falling clearly below the relation of Bouwens et al. (2016).

smaller sample do not affect the conclusions of Fudamoto et al. (2020a).

4.2. Shape of the attenuation curve

The combination of multi-wavelengths data with ALMA observations provides us with a unique opportunity to investigate the shape of attenuation curves at $z \sim 5$. As we saw in Sect. 4.1.2, the locus of ALPINE galaxies on the IRX-β diagram strongly suggests that there is a diversity of attenuation curves and that no single law can reproduce all of the observations.

4.2.1. Parametrization of the attenuation curve

How we quantify the shape of the attenuation curve is important if we want to study its variations. In CIGALE, we have modeled the attenuation adopting a starburst curve that is modified by a power law of index δ (Noll et al. 2009a, see Sect. 3.1). The strongest advantage of this parametrization is that δ is a direct indication of the steepness of the effective attenuation curve. In addition, because it can be used as a screen, it is easy to apply on observations to correct for the presence of dust. We emphasize, however, that the starburst curve itself does not account or assume any particular geometry. Rather, the effect of the geometry is statistically factored into it. A strong limitation of this curve, however, is that it does not explicitly take into account the additional reddening affecting star-forming regions, which can affect the steepness of the curve. In other words, the modified starburst curve empirically reproduces an effective attenuation curve but only gives limited information on the physics behind it.

The model of Charlot & Fall (2000) was specifically made to account for the differential attenuation between stars located in star forming regions (Birth Clouds, BC) and those in the ISM. The attenuation curve of each of these two components is described by a power law, with its own index, and the amount of dust associated with each component can also be variable. To make matters more complex, photons from stars in BC are attenuated both by the dust in the BC and the ISM, whereas stars not belonging to BC are only attenuated by the ISM component. This model is consistent with results from radiation transfer modeling (Chevallard et al. 2013; Buat et al. 2018) and has been remarkably successful to reproduce the observations and provides for a natural explanation for the shape of the starburst attenuation curve and deviations around it. As a consequence, it is frequently used in models. The main characteristic, however, is that there is only an indirect link between the shape of the attenuation curve of each component and the shape of the effective attenuation curve as would be measured from the observations. That is, the model of Charlot & Fall (2000) does not directly give an attenuation curve, unlike the modified Calzetti et al. (1994, 2000) curve (Noll et al. 2009a). Rather, even with fixed model parameters, the shape of the attenuation curve depends on the properties of the stellar populations, and therefore, on the SFH.

This being said, even though the Charlot & Fall (2000) model reproduces better the observations in the NIR (Lo Faro et al. 2017) and models based on radiation transfer computations (Chevallard et al. 2013), the level of flexibility of both curves is similar in the UV and optical domains and the Charlot & Fall (2000) model shines in a more theoretical setting such as numerical simulations and SED modeling. For this study, we have therefore decided to adopt the starburst curve for the modeling with CIGALE, as it allows for a simpler measurement of the shape of the attenuation curve through the δ index. We do, however, use the Charlot & Fall (2000) parametrization in Sect. 5 to inform on the physical interpretation of the results.

4.2.2. Relation between δ and A_V

To have a first glimpse of the attenuation in ALPINE galaxies, we show in Fig. 7 the range of attenuation curves in our sample in terms of amplitude and slope as parametrized through the index δ. An interesting property of our sample is the generally moderate attenuation of its members. We find that only two galaxies have a V-band attenuation larger than 1 magnitude. Even though the parent sample targets main-sequence galaxies selected in the UV, it is not surprising that some galaxies at higher attenuation are included, in particular among the more massive objects. These two galaxies are among the more massive of the sample with a stellar mass of $3.30 \times 10^{10}\,M_\odot$ and $4.26 \times 10^{10}\,M_\odot$, respectively. It is to be noted that by virtue of our selection, the objects must be detected with ALMA, which means that at fixed mass, our sample is naturally biased towards more dust-rich galaxies compared to the full ALPINE sample. This highlights both the sensitivity of the survey and the low dust content of main-sequence galaxies at $z \sim 5$. Another interesting finding is the large range of δ covered by the sample, from -1.84 to 0.23. We recall that a starburst curve corresponds to $\delta = 0$ and an SMC-like curve to $\delta \simeq -0.5$. This confirms our initial assessment from the inspection of the IRX-β diagram that the use of a single attenuation curve is not appropriate at $z \sim 5$. It is important to note that, as we see in Fig. 7, δ is not randomly distributed. Indeed, we find that there is a clear relation between the V-band attenuation and δ, with higher attenuation galaxies having a shallower attenuation curve. Such a variation is expected. It has been found in models and simulations (e.g., Witt & Gordon 2000; Chevallard et al. 2013; Seon & Draine 2016; Narayanan et al. 2018a; Trayford et al. 2020; Lin et al. 2021) as well as observationally (e.g., Salmon et al. 2016; Salim et al. 2018). We discuss this relation and its physical origin in Sect. 5.

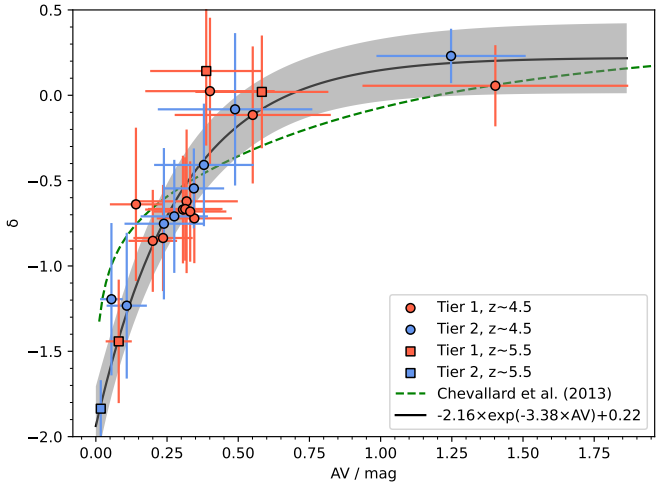


Fig. 7. Index δ of the power law modifying the starburst attenuation curve versus the V band attenuation. The symbols are identical to those of Fig. 3. The black line corresponds to the fit of a function of the form $a \times \exp(b \times A_V) + c$ using an orthogonal distance regression method, with the gray area representing the 1-σ dispersion. The dashed green line represents the model of Chevallard et al. (2013) as described in Sect. 5.2. We see that there is a clear relation between the V-band attenuation and δ, with higher attenuation galaxies having a shallower attenuation curve. Such a variation is expected. It has been found in models and simulations alike.

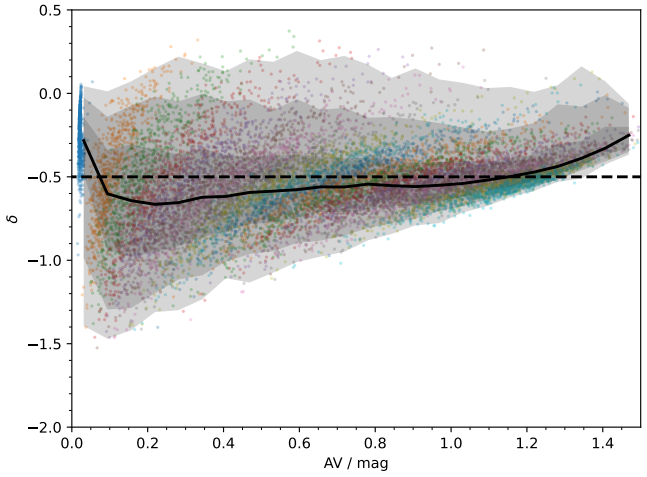


Fig. 8. Estimation of δ versus the V-band attenuation for a set of synthetic galaxies with fixed $\delta = -0.5$ (dashed black horizontal line) and a variable attenuation. Each value of the true reddening is plotted in a different color. The shaded areas represent the 1-, 2-, and 3-σ dispersion on δ, with the solid line indicating the median. The effect of the degeneracy is clearly visible for galaxies of the same true reddening. However, considering a range of attenuations, its effect is little different from a dispersion on δ with only a weak trend towards lower δ at low A_V. In addition, very few objects have an extremely steep δ, making it unlikely that they are generated due to degeneracies that would smear the results for a single attenuation curve.

5. Discussion

5.1. Impact of degeneracies

An important aspect to keep in mind in the rest of the article, however, is that δ and A_V are intrinsically degenerate with one another (see for instance the recent study of Qin et al. 2022). The strength of this degeneracy is directly linked to the extent of the multi-wavelength coverage and the uncertainties on the observations. A fair question, therefore, asks whether the relation we see in Fig. 7 would be driven by degeneracies rather than physics. In other words, we question whether we would obtain this relation if all galaxies followed the same attenuation curve but covered a range of A_V. To answer this question, we have generated a synthetic catalog from the best-fit models of our sample of 23 galaxies but setting a fixed $\delta = -0.5$ and an $E(B-V)$ reddening 0.005 mag to 0.5 mag in 20 steps. The set of bands and the relative uncertainties are taken to be identical to the observations of each galaxy, as are the redshifts. This is especially important as the results may vary significantly based on the bands used and their S/N, as mentioned above. This therefore allows us to reproduce the observed configuration as closely as possible. For each galaxy and each reddening, we generate 50 synthetic galaxies, injecting into each flux and the dust luminosity a random noise drawn from a normal distribution corresponding to the uncertainty in each band. The physical properties of each of these 23 000 galaxies are then evaluated in the same way as ALPINE galaxies, running CIGALE with the parameters given in Table 1. We show the results in Fig. 8. We see that the effect of the degeneracy between δ and A_V is clearly visible for galaxies with the same dust properties (points with the same color). However, considering a range of measurement attenuations, its effect is not very different from a dispersion on δ with only a weak trend towards lower δ at low A_V (as can be seen from the median). This variation is much smaller than the dynamical range of the relation. In addition, very few objects have an extremely steep δ, making it unlikely that they are generated due to degeneracies that would smear the results for a single attenuation curve. This being said, it is possible that considering a narrower range of A_V, therefore considering objects that are very similar in A_V, the local (as opposed to global) trends may be driven by the degeneracy. From these considerations, we think that the degeneracy stretches and amplifies the relation between δ and A_V to some degree. In reality it may be somewhat weaker but it is nevertheless real. It is necessary to remember this limitation when interpreting the results.

5.2. Dust properties and the δ-A_V relation

The broad diversity of attenuation curves in our homogeneous sample of 23 main-sequence galaxies is striking, going from curves shallower than starburst curves to steeper than SMC curves. At first sight, it may be surprising as these curves are often perceived as two extremes. However, the physical properties of the dust, the properties of the stellar populations, and the relative distribution of stars and dust all affect the shape of the attenuation curves, ultimately leading to the δ-A_V relation presented in Fig. 7.

A first aspect to consider is the relative distribution between stars and dust. Indeed, extinction curves are only valid in the case of a simple screen geometry. Through detailed radiation transfer simulations of a clumpy ISM, Seon & Draine (2016) showed that the attenuation curve can take a broad range of shapes depending on the properties of the dust and its distribution. The steepest curves are found at low column density, with the variation of the scattering albedo of the dust grains with wavelength playing a key role (Inoue et al. 2006; Seon & Draine 2016). To illustrate the steepening of the curve at low attenuation and the effect of the geometry we fit a modified starburst law to the radiation transfer models of Seon & Draine (2016) and we present in Fig. 9 the variation of δ as a function of the

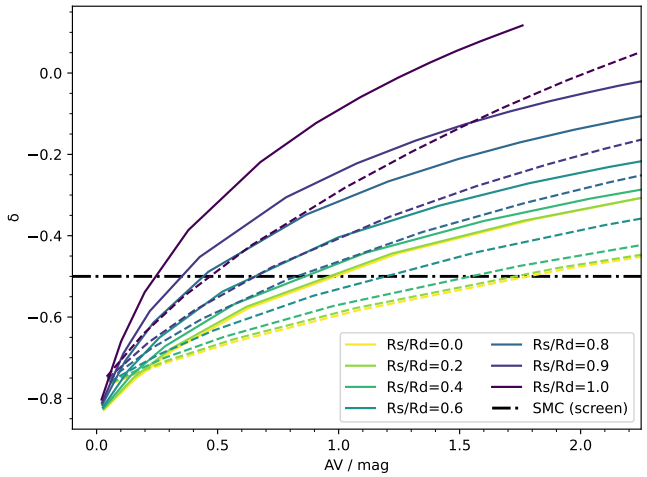


Fig. 9. Index δ of the power law modifying the starburst attenuation curve versus the V band attenuation for the clumpy ISM models of Seon & Draine (2016) with a Mach number of 4. Each colored line represents a model with a varying V-band optical depth and for a fixed distribution of stars and dust, parametrized by the ratio of their radii (Rs/Rd, for additional detail see Seon & Draine 2016). The solid lines represent a dust composition following the SMC dust model of Weingartner & Draine (2001) and the dashed lines that of Witt & Gordon (2000). The dash-dotted horizontal line indicates the slope of an SMC curve in the case of a pure screen geometry. We see that at fixed attenuation, the more extended the stellar distribution is compared to the dust, the flatter the attenuation curve is.

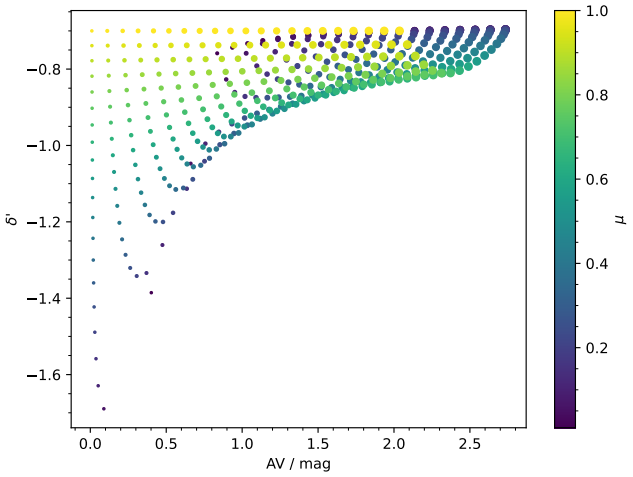


Fig. 10. Index δ' of the power law describing the effective attenuation curve versus the attenuation in the V band for the Charlot & Fall (2000) model. The size of the points is proportional to the V band ISM attenuation from 0.01 mag to 2 mag and the color gives μ, the fraction of the dust in the ISM following the color bar to the right of the figure. For reference, a starburst curve corresponds to $\delta' \simeq -0.7$. We see that in the low A_V and low μ regime, the attenuation curve can become much steeper.

attenuation and the geometry. The distribution of stars and dust is parametrized by the ratio of their radii, Rs/Rd. A value of 0 corresponds to a situation where the stars are centrally concentrated in the dust whereas a value of 1 corresponds to the stars and the dust following the same distribution. We see that at fixed attenuation, the more extended the stellar distribution is compared to the dust, the flatter the attenuation curve. This is because an increasingly larger fraction of the stars is located near the edge of the cloud, therefore a larger fraction of the stars will face a lower optical depth at shorter wavelengths as well. We also see that even though the specific dust models behind the SMC extinction curves (Weingartner & Draine 2001; Witt & Gordon 2000) do not yield exactly the same results, the general trend is driven by the geometry, with the steepest curves at the lowest attenuation.

It is also interesting to consider larger spatial scales. Displacements between the rest-frame UV and the rest-frame dust emission (e.g., Hodge et al. 2016; Tadaki et al. 2017; Gómez-Guijarro et al. 2018; Puglisi et al. 2019) can lead to changes in the attenuation curves. These offsets do not appear to affect modeling negatively (Buat et al. 2019). However, as shown in Fujimoto et al. (2020) the offsets in ALPINE galaxies appear small or altogether absent, so displacements should not play a major role in the evolution of attenuation curves in our sample. This being said, a number of ALPINE galaxies are mergers (Le Fèvre et al. 2020; Jones et al. 2020, 2021) and most of these sources are likely undergoing inflows or unresolved minor mergers. This is also true for our subsample. This is likely to have some degree of influence. However, our sample is too small to split into subsamples based on the morpho-kinematic properties to investigate whether this would have a systematic influence.

Another mechanism that can lead to attenuation curves steeper than the intrinsic extinction curves is the effect of the differential reddening between different stellar populations (Inoue 2005). This is the case because star-forming regions generally account for a much larger fraction of the luminosity in the UV than at longer wavelengths. Because star-forming regions are dustier than the general ISM, there is a transition from low attenuation populations in the near-infrared and in the optical to high-attenuation populations in the UV. While the details of the dust properties and its spatial distribution described above are difficult to assess in this work, we can easily quantify the effect of the differential reddening, which fits very well within the framework of the Charlot & Fall (2000) models that we previously described (see also Lin et al. 2021). To quantify the degree of steepening that differential reddening can bring, we built a simple model with CIGALE: a fixed delayed SFH (age of 1.3 Gyr, τ of 500 Myr, and a burst fraction of 5%, with the other parameters as described in Table 1), stellar populations with a metallicity $Z = 0.008$, following a Chabrier (2003) IMF, and the Charlot & Fall (2000) model. The latter has four parameters: the indices of the attenuation curves of the BC and of the ISM, which are described by power laws and that we set to constant values of $n_{\rm BC} = -1.3$ and $n_{\rm ISM} = -0.7$ respectively, following Charlot & Fall (2000), the V-band attenuation of the ISM, and μ, which is defined as the ratio of the ISM attenuation to the sum of the attenuation from the ISM and BC, all in the V band.

In order to illustrate the effect of the steepening of the slope due to differential reddening, as a starting point, we consider a fairly attenuated galaxy for which we take $\mu = 1$ (i.e., all the dust is located in the ISM), with an ISM V-band attenuation of 1 mag. Fitting the resulting effective attenuation curve with a power law of index δ' between 150 nm and 800 nm, we retrieve as expected a power law of index $\delta' \simeq -0.7$, which is similar to the starburst curve (in this formulation, $\delta' \simeq \delta - 0.7$). We show the effect of varying both the ISM attenuation and μ in Fig. 10.

Quantitatively, if we reduce μ to 0.5 (half the dust is located in BC), the effective slope steepens to $\delta' = -1.07$ and the effective V-band attenuation increases to 1.35 mag. If we now reduce the ISM attenuation to 0.25 mag, the slope steepens to

$\delta' = -1.22$, slightly steeper than an SMC curve. In turn, reducing μ to 1/3 (that is, 2/3 of the dust is located in BC) while keeping the ISM attenuation of 0.25 mag yields $\delta' = -1.38$. A more extreme combination of $\mu = 0.1$ (90% of the dust is located in BC) with an ISM attenuation of 0.1 mag corresponds to $\delta' = -1.59$ for an effective V-band attenuation of 0.43 mag. While the steepening reaches nearly 0.9 dex compared to a starburst curve, it is not clear whether such low μ are realistic, even at high redshift. However, given the young age of these galaxies and their gas-rich nature, it is probably reasonable to consider that dust may remain confined more efficiently in the vicinity of star-forming regions and that it is dispersed much less efficiently than it would in more gas-poor galaxies, leaving the general ISM relatively dust free, as compared to star-forming regions.

Another aspect not to neglect in the previous paragraph is the choice of $n_{\rm BC}$ and $n_{\rm ISM}$ in the Charlot & Fall (2000) models. Steeper $n_{\rm BC}$ and $n_{\rm ISM}$ naturally yield steeper effective attenuation curves. We also need to consider a possible variation of $n_{\rm ISM}$ with the attenuation. Adopting the stellar populations described above, $\mu = 1/3$ and the dependence of $n_{\rm ISM}$ on the attenuation derived in Chevallard et al. (2013), we see in Fig. 7 that their model appears to broadly reproduce the general trend and amplitude of the variations.

The SMC extinction curve, the steepest curve we can measure in the local universe, is not a single curve but rather a mean curve over a variety of regions that can be observed across the SMC. It is therefore reasonable to consider that there could be steeper curves, in particular at high redshift, where the physical conditions can differ from that of the SMC, yielding different composition and size distribution. Evidence towards the existence of extinction curves in distant galaxies at least as steep as that of the SMC can be found in observations of quasars and γ-ray bursts (Zafar et al. 2015, 2018). They are specific cases where we can measure the extinction curve beyond the local universe thanks to their point-like nature that allows to eliminate geometrical effects.

Finally, changes in the properties of the attenuation may be related with the metallicity of the ISM. In a study of redshift 2.0–2.5 galaxies, Shivaei et al. (2020) found that galaxies with a lower metallicity tend to have a steeper attenuation curve. While we do not know the metallicity of the galaxies in our sample, their young age and gas-rich nature suggest that they tend to be on the lower side, which would go towards having steeper curves.

From the above description, we see that there are multiple mechanisms at play that can result in the steepening of the slope at lower attenuation. However, it appears unlikely that any single process can explain by itself the particularly steep slopes we find at the lowest attenuation. In their recent study, Lin et al. (2021) combined dust grain growth models with radiation transfer computations of one and two-zone geometries of galaxies at very high redshift, showing how different processes can act together, yielding attenuation curves considerably steeper than the extinction curve. More generally, hydrodynamical simulations of galaxies such as those presented in Narayanan et al. (2018a; see in particular panel C of Fig. 6 in Salim & Narayanan 2020) or Trayford et al. (2020; see in particular their Fig. 5) that combine radiation transfer computations with complex stellar populations and geometries are in excellent agreement with the overall trend that we observe in our sample. Ultimately, the combination of steep extinction curves at high redshift, the effect of the geometry, and differential reddening probably results in the increasingly steep attenuation curves we measure in lower attenuation galaxies in our sample.

5.3. Impact of adopting a single attenuation curve

The large range of attenuation curves necessarily has an impact on our capacity to reliably correct SFR estimators for the presence of dust. As mentioned earlier, the UV slope β is one of the main tracers of the attenuation. Assuming sufficiently deep observations and a narrow range in the intrinsic slope β_0, the variation of the attenuation curve can be the main source of uncertainty. To quantify the effect of the dependence of the shape of the attenuation curve on A_V, we first built a simple model with a fixed β_0, which we attenuate with a full range of attenuation curves from $\delta = -1.8$ to $\delta = 0.5$. We then interpolate these models following the relation between δ and A_V shown in Fig. 7. We show the resulting variation of β as a function of the attenuation in Fig. 11.

We immediately see that the evolution of β with the attenuation follows a very different track compared to the starburst and SMC curves. If we consider a fixed attenuation curve, β becomes monotonically redder, more (SMC) or less (starburst) rapidly. However, if δ depends on the attenuation, β rapidly becomes redder, even at low attenuation, peaking a bit below $\beta = -0.8$ between 0.1 and 0.2 mag before slowly decreasing until A_V reaches slightly under 1 mag and then increases again but more slowly than in the case of a starburst curve, while always staying below $\beta = -0.5$ for an attenuation lower than 2.5 mag. The evolution of β with the attenuation is not as dramatic in the FUV. It increases monotonically but not at the constant rate of fixed attenuation curves. We also observe a similar transition from curves steeper than the SMC at low attenuation to shallower than starburst at higher attenuation.

The direct consequence of the aforementioned relation is that, in the case of main-sequence galaxies at $z \sim 5$, β cannot easily be used to infer the attenuation of galaxies. Naturally, the magnitude of this issue depends on the exact relation between δ and A_V. An important question is its behavior at higher attenuation. We see in Fig. 7 that this relation is constrained by only two galaxies with an attenuation larger than 1 magnitude that both have $\delta > 0$. The starburst curve already being fairly gray, even a moderate flattening with a positive δ rapidly makes it that dust only has little reddening effect, leaving even dusty galaxies quite blue. In effect, this means that the blue color of high-redshift galaxies is not necessarily proof that they would harbor little dust. As we see, the question of the asymptotic convergence of δ bears important consequences. If in our case, the reliance on only a couple of data points does not allow us to draw a firm conclusion, it is interesting to note that Salmon et al. (2016) also found $\delta > 0$ at higher attenuation. This is in agreement with the radiation transfer models of Witt & Gordon (2000), Seon & Draine (2016) as well as the simulations of Narayanan et al. (2018a), Trayford et al. (2020), which show that this possibility needs to be taken into account when interpreting observations of dusty galaxies.

At lower attenuation, a possible bias to consider is that, all things being equal, we preferentially select galaxies with steeper curves as they have a higher dust luminosity and the uncertainty on δ is smaller. In that sense, it is possible that the variation of δ with respect to the attenuation would not be as fast in the sense that there could be galaxies at low attenuation with larger δ. However, even if that is the case, we still expect a variation (see Sect. 5.2) and our sample shows that at least some main-sequence galaxies have a very steep δ, shedding doubt on whether even for an homogeneous set of galaxies a single relation would be appropriate.

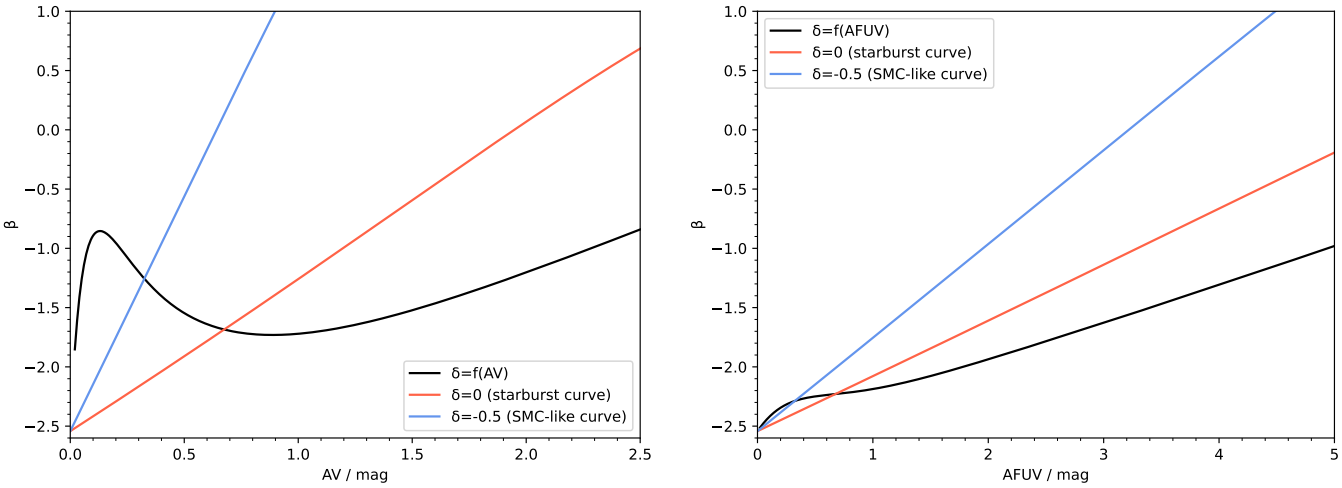


Fig. 11. Observed UV slope β as a function of the V-band (*left*) and FUV (*right*) attenuation (black), assuming the relation between the attenuation curve slope δ and the attenuation shown in Fig. 7. For comparison the evolution of β for starburst and SMC-like attenuation curves are shown in red and blue, respectively. We see that the evolution of β with the attenuation follows a very different track compared to the starburst and SMC curves. The consequence is that, in the case of main-sequence galaxies at $z \sim 5$, β cannot easily be used to infer the attenuation of galaxies

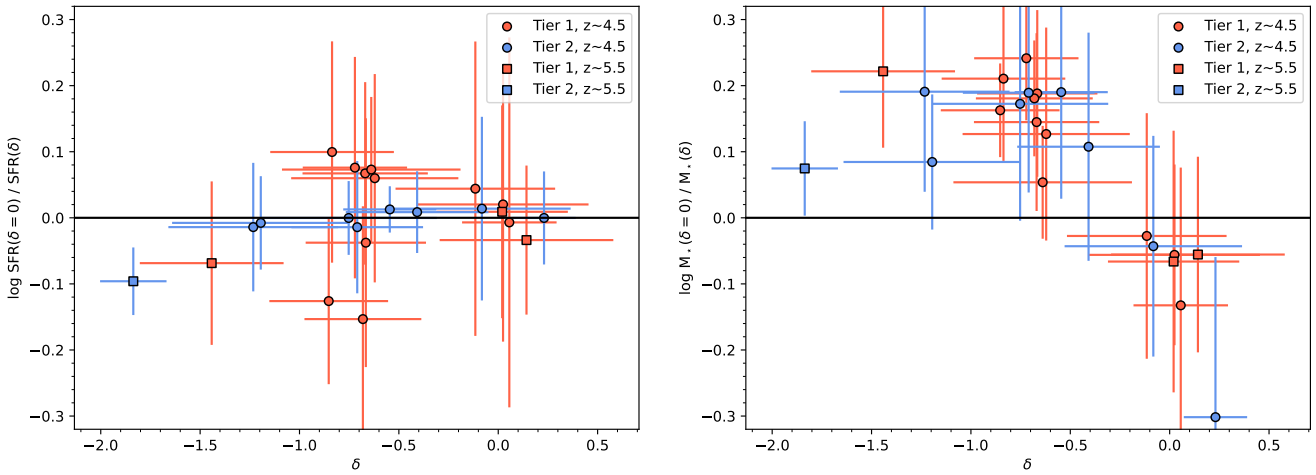


Fig. 12. Ratio of the estimated SFR (*left*) and $M_\star$ (*right*) when setting $\delta = 0$ and leaving δ free. The symbols are identical to those of Fig. 3.

Finally, a fair question is the magnitude of the impact when adopting a fixed attenuation curve for estimating the SFR and $M_\star$ from SED modeling. To evaluate this, we have fitted again the sample but this time setting $\delta = 0$. We find that the difference and the corresponding dispersion are fairly small: $\Delta \log \mathrm{SFR}/(M_\odot\,\mathrm{yr}^{-1}) = 0.00 \pm 0.06$ and $\Delta \log M_\star/M_\odot = 0.08 \pm 0.14$ (Fig. 12). The reason the difference in the estimates is minute for the SFR is probably three-fold. First, we do not consider the full range of possible variations of the recent SFH since the data at our disposal are not sufficient to constrain such variations. For instance the shortest timescales would ideally be probed with an hydrogen recombination line. At the same time, the constraint from the [C II] emission through the SFR limits deviations from the input value. However, there is also probably a more physical reason to this. Most of the energy emitted by the dust is absorbed in the UV. This is especially the case for actively star-forming galaxies at high redshift for which the influence of dust heating by evolved stellar populations is naturally more limited than at lower redshift. It comes that the key property to retrieve the SFR is the amplitude of the attenuation curve in the UV rather than its exact shape. For $M_\star$, the difference in the estimates follows a clear trend with δ. As energy balance is a critical factor to set the amplitude of the UV attenuation, the shape of the curve will gain importance when determining other physical properties such as $M_\star$. Having a fixed attenuation curve means that the optical-to-NIR attenuation will be strongly determined by the UV attenuation, which – even at these high redshifts – is not appropriate.

Ultimately, the strong dependence of δ on the attenuation has a dramatic and complex effect on the emerging emission from galaxies. We therefore strongly recommend utmost caution when using β to correct for dust attenuation at $z \sim 5$, as there are considerable uncertainties on the shape of attenuation curves.

This being said, as we have seen in Fig. 12, the impact of using a fixed attenuation curve remains fairly limited when using SED modeling. No clear effect is seen on the SFR, most likely because the determination of AFUV, which is the critical factor for this, is less sensitive to the exact shape of the attenuation curve than A_V. In effect, the choice of the attenuation curve is more impactful for measuring the stellar mass, with a systematic trend. The mass offset remains limited to 0.3 dex, however. In conclusion, the physical cause of these variations requires

further study; for instance, spatially resolved observations with ALMA and JWST will allow for the exploration of whether the large-scale geometries of these objects could explain such variations in their attenuation curves. Thus, the conclusion of our study is that practical effects remain sufficiently contained such that using a single attenuation curve may be sufficient for many studies as long as SED modeling can be employed.

6. Summary and conclusion

In this work, we studied 23 main-sequence $z = 4.4$–5.5 galaxies from the ALPINE survey to measure the dust attenuation properties in general and the shape of the attenuation curves in particular. To do so, we used the CIGALE code to model the SED in at least six rest-frame UV-to-optical bands in addition to the dust luminosity or the [C II] luminosity. These models are based on a delayed+burst SFH, the stellar populations of Charlot & Fall (2000), and a power law-modified starburst attenuation curve allowing a broad range of shapes. We find the following.

- The relations between SFR, $M_\star$, IRX, and β (see Figs. 4–6) are broadly consistent with the findings of Fudamoto et al. (2020a), who used the LePhare code but without including constraints from the ALMA observations.
- These relations suggest, however, that there exists a variety of attenuation curves in main-sequence galaxies at $z \sim 5$.
- Estimating the index δ of the power law modifying the starburst attenuation curve, we find it ranges from $\delta = -1.84$ to $\delta = 0.23$ (Table B.1). For reference, $\delta = 0$ corresponds to a bona fide starburst curve and $\delta = -0.5$ to an SMC-like extinction curve.
- The index δ is strongly dependent on the V-band attenuation, with steeper curves corresponding to lower attenuation (Fig. 7).
- It is likely that the steeper curves are the product of a combination of intrinsically steep extinction curves, the effect of the dust distribution, and differential reddening between star-forming regions and the ISM (see Figs. 9 and 10).
- Ultimately, there is no single attenuation curve that is appropriate for all high-redshift main-sequence galaxies. Caution is strongly advised when interpreting the UV color in terms of attenuation. However, when SED modeling is available, the impact of the choice of the attenuation curve on the SFR and $M_\star$ is limited (Figs. 11 and 12).

Over the next few years, the combination of high-resolution ALMA and JWST data will be instrumental in gaining a better understanding of the physical processes that give rise to steep attenuation curves in galaxies.

Acknowledgements. We would like to thank the referee for their very insightful comments that we believe have helped clarify and improve our article. Médéric Boquien gratefully acknowledges support by the ANID BASAL project FB210003 and from the FONDECYT regular grants 1170618 and 1211000. D.N. acknowledges funding from the Space Telescope Science Institute via grant AR-15043.001. G.C.J. acknowledges ERC Advanced Grant 695671 "QUENCH" and support by the Science and Technology Facilities Council (STFC). This research made use of Astropy, (`http://www.astropy.org`) a community-developed core Python package for Astronomy (Astropy Collaboration 2013, 2018).

References

Álvarez-Márquez, J., Burgarella, D., Heinis, S., et al. 2016, A&A, 587, A122
Álvarez-Márquez, J., Burgarella, D., Buat, V., Ilbert, O., & Pérez-González, P. G. 2019, A&A, 630, A153
Arnouts, S., Cristiani, S., Moscardini, L., et al. 1999, MNRAS, 310, 540
Astropy Collaboration (Robitaille, T. P., et al.) 2013, A&A, 558, A33
Astropy Collaboration (Price-Whelan, A. M., et al.) 2018, AJ, 156, 123
Atek, H., Siana, B., Scarlata, C., et al. 2011, ApJ, 743, 121
Barisic, I., Faisst, A. L., Capak, P. L., et al. 2017, ApJ, 845, 41
Béthermin, M., Fudamoto, Y., Ginolfi, M., et al. 2020, A&A, 643, A2
Bogdanoska, J., & Burgarella, D. 2020, MNRAS, 496, 5341
Boquien, M., Duc, P., Wu, Y., et al. 2009, AJ, 137, 4561
Boquien, M., Buat, V., Boselli, A., et al. 2012, A&A, 539, A145
Boquien, M., Kennicutt, R., Calzetti, D., et al. 2016, A&A, 591, A6
Boquien, M., Burgarella, D., Roehlly, Y., et al. 2019, A&A, 622, A103
Bouwens, R. J., Aravena, M., Decarli, R., et al. 2016, ApJ, 833, 72
Brammer, G. B., van Dokkum, P. G., Franx, M., et al. 2012, ApJS, 200, 13
Brinchmann, J., Charlot, S., White, S. D. M., et al. 2004, MNRAS, 351, 1151
Bruzual, G., & Charlot, S. 2003, MNRAS, 344, 1000
Buat, V., Boselli, A., Gavazzi, G., & Bonfanti, C. 2002, A&A, 383, 801
Buat, V., Iglesias-Páramo, J., Seibert, M., et al. 2005, ApJ, 619, L51
Buat, V., Takeuchi, T. T., Burgarella, D., Giovannoli, E., & Murata, K. L. 2009, A&A, 507, 693
Buat, V., Noll, S., Burgarella, D., et al. 2012, A&A, 545, A141
Buat, V., Boquien, M., Małek, K., et al. 2018, A&A, 619, A135
Buat, V., Ciesla, L., Boquien, M., Małek, K., & Burgarella, D. 2019, A&A, 632, A79
Burgarella, D., Buat, V., & Iglesias-Páramo, J. 2005, MNRAS, 360, 1413
Burgarella, D., Nanni, A., Hirashita, H., et al. 2020, A&A, 637, A32
Calzetti, D., Kinney, A. L., & Storchi-Bergmann, T. 1994, ApJ, 429, 582
Calzetti, D., Armus, L., Bohlin, R. C., et al. 2000, ApJ, 533, 682
Capak, P. L., Carilli, C., Jones, G., et al. 2015, Nature, 522, 455
Casey, C. M., Scoville, N. Z., Sanders, D. B., et al. 2014, ApJ, 796, 95
Cassata, P., Morselli, L., Faisst, A., et al. 2020, A&A, 643, A6
Chabrier, G. 2003, ApJ, 586, L133
Charlot, S., & Fall, S. M. 2000, ApJ, 539, 718
Chevallard, J., Charlot, S., Wandelt, B., & Wild, V. 2013, MNRAS, 432, 2061
Ciesla, L., Elbaz, D., & Fensch, J. 2017, A&A, 608, A41
Cullen, F., McLure, R. J., Khochfar, S., Dunlop, J. S., & Dalla Vecchia, C. 2017, MNRAS, 470, 3006
Dessauges-Zavadsky, M., Ginolfi, M., Pozzi, F., et al. 2020, A&A, 643, A5
Di Mascia, F., Gallerani, S., Ferrara, A., et al. 2021, MNRAS, 506, 3946
Eldridge, J. J., & Stanway, E. R. 2009, MNRAS, 400, 1019
Faisst, A. L., Capak, P. L., Davidzon, I., et al. 2016, ApJ, 822, 29
Faisst, A. L., Capak, P. L., Yan, L., et al. 2017, ApJ, 847, 21
Faisst, A. L., Schaerer, D., Lemaux, B. C., et al. 2020, ApJS, 247, 61
Fudamoto, Y., Oesch, P. A., Schinnerer, E., et al. 2017, MNRAS, 472, 483
Fudamoto, Y., Oesch, P. A., Magnelli, B., et al. 2020a, MNRAS, 491, 4724
Fudamoto, Y., Oesch, P. A., Faisst, A., et al. 2020b, A&A, 643, A4
Fujimoto, S., Silverman, J. D., Bethermin, M., et al. 2020, ApJ, 900, 1
Giacconi, R., Zirm, A., Wang, J., et al. 2002, ApJS, 139, 369
Ginolfi, M., Jones, G. C., Béthermin, M., et al. 2020, A&A, 633, A90
Giovannoli, E., Buat, V., Noll, S., Burgarella, D., & Magnelli, B. 2011, A&A, 525, A150
Gómez-Guijarro, C., Toft, S., Karim, A., et al. 2018, ApJ, 856, 121
Grogin, N. A., Kocevski, D. D., Faber, S. M., et al. 2011, ApJS, 197, 35
Gruppioni, C., Béthermin, M., Loiacono, F., et al. 2020, A&A, 643, A8
Hao, C.-N., Kennicutt, R. C., Johnson, B. D., et al. 2011, ApJ, 741, 124
Heinis, S., Buat, V., Béthermin, M., et al. 2014, MNRAS, 437, 1268
Hodge, J. A., Swinbank, A. M., Simpson, J. M., et al. 2016, ApJ, 833, 103
Howell, J. H., Armus, L., Mazzarella, J. M., et al. 2010, ApJ, 715, 572
Ilbert, O., Arnouts, S., McCracken, H. J., et al. 2006, A&A, 457, 841
Inoue, A. K. 2005, MNRAS, 359, 171
Inoue, A. K., Iwata, I., & Deharveng, J.-M. 2006, MNRAS, 371, L1
Jones, G. C., Béthermin, M., Fudamoto, Y., et al. 2020, MNRAS, 491, L18
Jones, G. C., Vergani, D., Romano, M., et al. 2021, MNRAS, 507, 3540
Kennicutt, R. C., & Evans, N. J. 2012, ARA&A, 50, 531
Khusanova, Y., Bethermin, M., Le Fèvre, O., et al. 2021, A&A, 649, A152
Koekemoer, A. M., Faber, S. M., Ferguson, H. C., et al. 2011, ApJS, 197, 36
Kong, X., Charlot, S., Brinchmann, J., & Fall, S. M. 2004, MNRAS, 349, 769
Koprowski, M. P., Coppin, K. E. K., Geach, J. E., et al. 2018, MNRAS, 479, 4355
Koprowski, M. P., Coppin, K. E. K., Geach, J. E., et al. 2020, MNRAS, 492, 4927
Kroupa, P. 2001, MNRAS, 322, 231
Laigle, C., McCracken, H. J., Ilbert, O., et al. 2016, ApJS, 224, 24
Le Fèvre, O., Béthermin, M., Faisst, A., et al. 2020, A&A, 643, A1
Leitherer, C., Li, I.-H., Calzetti, D., & Heckman, T. M. 2002, ApJS, 140, 303
Liang, L., Feldmann, R., Hayward, C. C., et al. 2021, MNRAS, 502, 3210
Lin, Y.-H., Hirashita, H., Camps, P., & Baes, M. 2021, MNRAS, 507, 2755
Lo Faro, B., Buat, V., Roehlly, Y., et al. 2017, MNRAS, 472, 1372
Loiacono, F., Decarli, R., Gruppioni, C., et al. 2021, A&A, 646, A76
Lower, S., Narayanan, D., Leja, J., et al. 2020, ApJ, 904, 33
Madau, P., & Dickinson, M. 2014, ARA&A, 52, 415

Mancini, M., Schneider, R., Graziani, L., et al. 2016, MNRAS, 462, 3130
Meiksin, A. 2006, MNRAS, 365, 807
Meurer, G. R., Heckman, T. M., & Calzetti, D. 1999, ApJ, 521, 64
Michałowski, M. J. 2015, A&A, 577, A80
Narayanan, D., Davé, R., Johnson, B. D., et al. 2018a, MNRAS, 474, 1718
Narayanan, D., Conroy, C., Davé, R., Johnson, B. D., & Popping, G. 2018b, ApJ, 869, 70
Noeske, K. G., Weiner, B. J., Faber, S. M., et al. 2007, ApJ, 660, L43
Noll, S., Pierini, D., Cimatti, A., et al. 2009a, A&A, 499, 69
Noll, S., Burgarella, D., Giovannoli, E., et al. 2009b, A&A, 507, 1793
Péroux, C., & Howk, J. C. 2020, ARA&A, 58, 363
Popping, G., Puglisi, A., & Norman, C. A. 2017, MNRAS, 472, 2315
Pozzi, F., Calura, F., Fudamoto, Y., et al. 2021, A&A, 653, A84
Puglisi, A., Daddi, E., Liu, D., et al. 2019, ApJ, 877, L23
Qin, J., Zheng, X. Z., Fang, M., et al. 2022, MNRAS, 511, 765
Reddy, N. A., Erb, D. K., Pettini, M., Steidel, C. C., & Shapley, A. E. 2010, ApJ, 712, 1070
Reddy, N., Dickinson, M., Elbaz, D., et al. 2012, ApJ, 744, 154
Reddy, N. A., Kriek, M., Shapley, A. E., et al. 2015, ApJ, 806, 259
Reddy, N. A., Steidel, C. C., Pettini, M., & Bogosavljević, M. 2016, ApJ, 828, 107
Reddy, N. A., Oesch, P. A., Bouwens, R. J., et al. 2018, ApJ, 853, 56
Riechers, D. A., Bradford, C. M., Clements, D. L., et al. 2013, Nature, 496, 329
Romano, M., Cassata, P., Morselli, L., et al. 2021, A&A, 653, A111
Romano, M., Cassata, P., Morselli, L., et al. 2020, MNRAS, 496, 875
Salim, S., & Boquien, M. 2019, ApJ, 872, 23
Salim, S., & Narayanan, D. 2020, ARA&A, 58, 529
Salim, S., Boquien, M., & Lee, J. C. 2018, ApJ, 859, 11
Salmon, B., Papovich, C., Long, J., et al. 2016, ApJ, 827, 20
Sargent, W. L. W., & Searle, L. 1970, ApJ, 162, L155
Sargsyan, L., Lebouteiller, V., Weedman, D., et al. 2012, ApJ, 755, 171
Sargsyan, L., Samsonyan, A., Lebouteiller, V., et al. 2014, ApJ, 790, 15
Sawicki, M. 2012, PASP, 124, 1208
Schaerer, D., Ginolfi, M., Béthermin, M., et al. 2020, A&A, 643, A3
Scoville, N., Aussel, H., Brusa, M., et al. 2007, ApJS, 172, 1
Scoville, N., Faisst, A., Capak, P., et al. 2015, ApJ, 800, 108
Seibert, M., Martin, D. C., Heckman, T. M., et al. 2005, ApJ, 619, L55
Seon, K.-I., & Draine, B. T. 2016, ApJ, 833, 201
Shivaei, I., Reddy, N. A., Steidel, C. C., & Shapley, A. E. 2015, ApJ, 804, 149
Shivaei, I., Darvish, B., Sattari, Z., et al. 2020, ApJ, 903, L28
Skelton, R. E., Whitaker, K. E., Momcheva, I. G., et al. 2014, ApJS, 214, 24
Speagle, J. S., Steinhardt, C. L., Capak, P. L., & Silverman, J. D. 2014, ApJS, 214, 15
Tadaki, K.-I., Genzel, R., Kodama, T., et al. 2017, ApJ, 834, 135
Trayford, J. W., Lagos, C. d. P., Robotham, A. S. G., & Obreschkow, D. 2020, MNRAS, 491, 3937
Watson, D., Christensen, L., Knudsen, K. K., et al. 2015, Nature, 519, 327
Weingartner, J. C., & Draine, B. T. 2001, ApJ, 548, 296
Whitaker, K. E., Franx, M., Leja, J., et al. 2014, ApJ, 795, 104
Witt, A. N., & Gordon, K. D. 2000, ApJ, 528, 799
Xu, C. K., Shupe, D., Buat, V., et al. 2007, ApJS, 173, 432
Yan, L., Sajina, A., Loiacono, F., et al. 2020, ApJ, 905, 147
Yuan, F.-T., Burgarella, D., Corre, D., et al. 2019, A&A, 631, A123
Zafar, T., Møller, P., Watson, D., et al. 2015, A&A, 584, A100
Zafar, T., Watson, D., Møller, P., et al. 2018, MNRAS, 479, 1542

Appendix A: Best fits

We show in Fig. A.1 and A.2 the best fits for each for the tier 1 and tier 2 galaxies in our final sample.

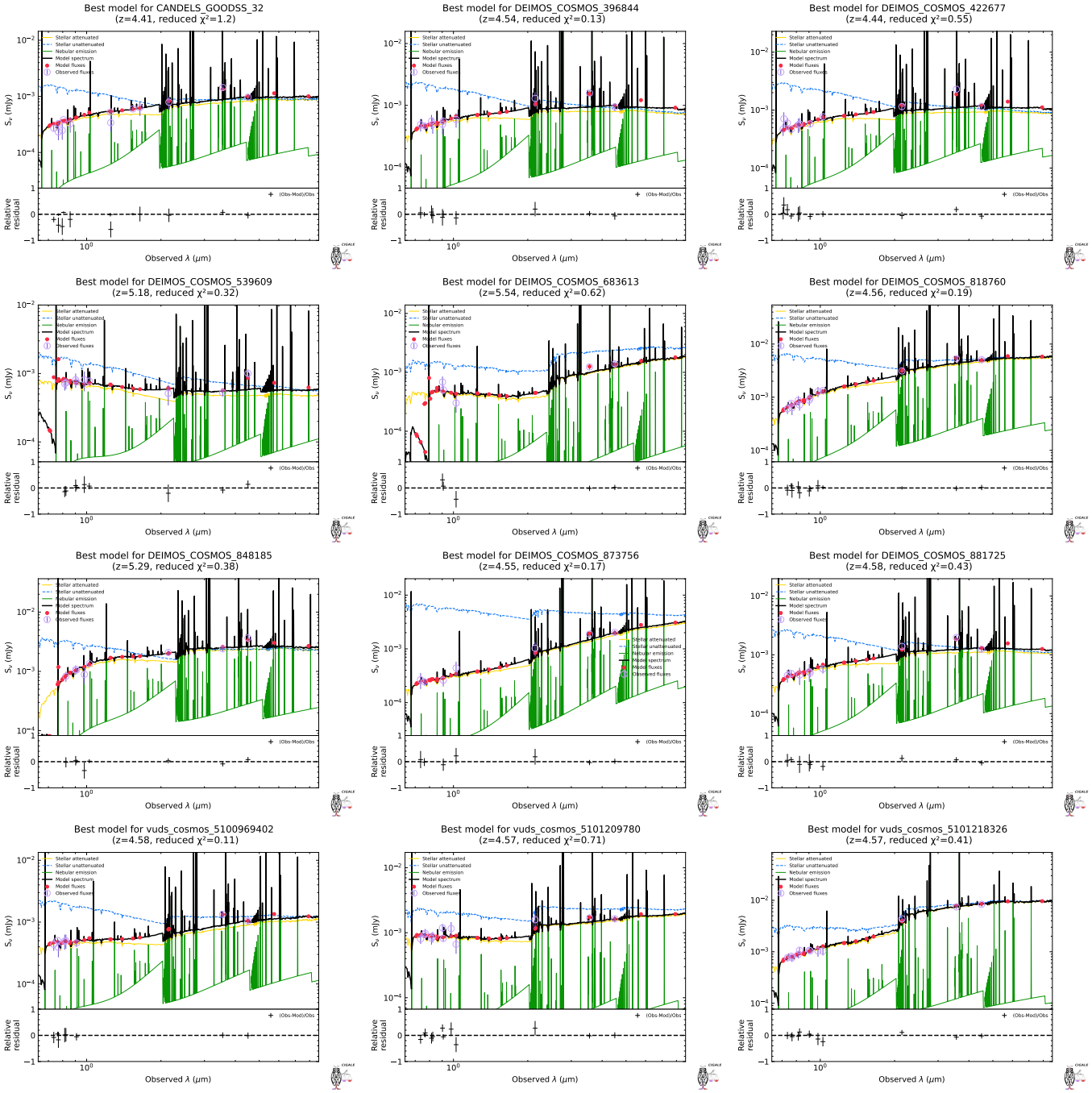


Fig. A.1. Best fits for tier 2 galaxies (except for vuds_cosmos_5180966608 and vuds_efdcs_530029038, which are shown in Fig. 2). The galaxy spectrum is shown in black, with the dust-attenuated stellar populations in yellow and the ionized gas in green. For comparison, the dust-free stellar populations are shown in blue. The model fluxes integrated in passbands are shown as red circles and the observations and 1-σ uncertainties are indicated with purple circles with vertical lines. Finally the relative residuals are shown in the bottom panel of each plot.

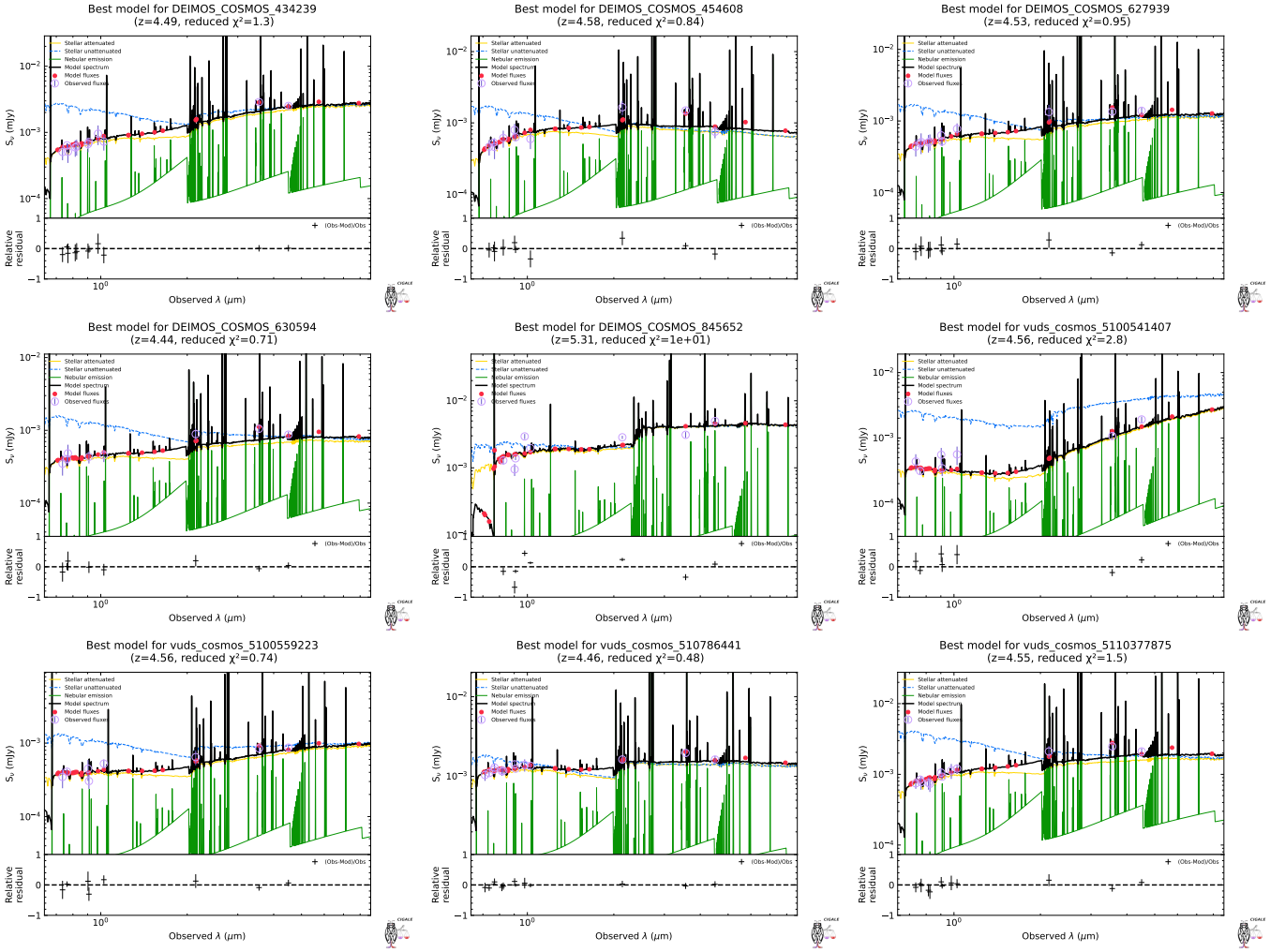


Fig. A.2. Best fits for tier 1 galaxies. The galaxy spectrum is shown in black, with the dust-attenuated stellar populations in yellow and the ionized gas in green. For comparison, the dust-free stellar populations are shown in blue. The model fluxes integrated in passbands are shown as red circles and the observations and 1-σ uncertainties are indicated with purple circles with vertical lines. Finally the relative residuals are shown in the bottom panel of each plot.

Appendix B: Physical properties

We present in Table B.1 the main physical properties of our sample.

Table B.1. Physical properties and corresponding uncertainties for the galaxies in our sample.

Name	Tier	z	IRX	β	δ	AFUV mag	A_V mag	SFR $M_\odot\ yr^{-1}$	$M_\star$ $M_\odot$
CANDELS_GOODSS_32	1	4.41	0.57 ± 0.14	−1.20 ± 0.08	−0.84 ± 0.31	1.46 ± 0.24	0.24 ± 0.10	50.86 ± 15.89	$7.52 \times 10^9 \pm 1.83 \times 10^9$
DEIMOS_COSMOS_396844	1	4.54	0.57 ± 0.14	−1.44 ± 0.24	−0.62 ± 0.42	1.42 ± 0.23	0.32 ± 0.18	76.88 ± 18.75	$7.84 \times 10^9 \pm 2.27 \times 10^9$
DEIMOS_COSMOS_422677	1	4.44	0.63 ± 0.11	−1.29 ± 0.20	−0.67 ± 0.32	1.54 ± 0.20	0.31 ± 0.13	91.97 ± 18.88	$8.43 \times 10^9 \pm 1.92 \times 10^9$
DEIMOS_COSMOS_539609	1	5.18	0.07 ± 0.22	−2.42 ± 0.11	0.14 ± 0.44	0.67 ± 0.21	0.39 ± 0.20	66.52 ± 13.38	$5.41 \times 10^9 \pm 1.46 \times 10^9$
DEIMOS_COSMOS_683613	1	5.54	0.51 ± 0.17	−1.90 ± 0.22	0.02 ± 0.33	1.28 ± 0.26	0.58 ± 0.23	54.64 ± 14.19	$1.95 \times 10^{10} \pm 7.70 \times 10^9$
DEIMOS_COSMOS_818760	1	4.56	0.81 ± 0.14	−0.74 ± 0.17	−0.72 ± 0.26	1.94 ± 0.26	0.35 ± 0.13	159.53 ± 53.88	$5.07 \times 10^{10} \pm 9.63 \times 10^9$
DEIMOS_COSMOS_848185	1	5.29	0.32 ± 0.09	−1.20 ± 0.17	−1.44 ± 0.36	1.05 ± 0.14	0.08 ± 0.05	120.35 ± 30.07	$2.42 \times 10^{10} \pm 5.32 \times 10^9$
DEIMOS_COSMOS_873756	1	4.55	1.36 ± 0.22	−1.31 ± 0.31	0.06 ± 0.24	3.03 ± 0.49	1.40 ± 0.47	142.62 ± 66.46	$4.26 \times 10^{10} \pm 1.88 \times 10^{10}$
DEIMOS_COSMOS_881725	1	4.58	0.66 ± 0.13	−1.20 ± 0.22	−0.67 ± 0.30	1.60 ± 0.23	0.31 ± 0.13	87.12 ± 23.58	$1.04 \times 10^{10} \pm 2.50 \times 10^9$
vuds_cosmos_5100969402	1	4.58	0.54 ± 0.19	−1.85 ± 0.25	−0.12 ± 0.40	1.36 ± 0.30	0.55 ± 0.27	59.00 ± 21.63	$1.24 \times 10^{10} \pm 4.58 \times 10^9$
vuds_cosmos_5101209780	1	4.57	0.17 ± 0.26	−2.16 ± 0.15	0.02 ± 0.43	0.81 ± 0.28	0.40 ± 0.23	54.90 ± 18.01	$1.84 \times 10^{10} \pm 4.73 \times 10^9$
vuds_cosmos_5101218326	1	4.57	0.51 ± 0.14	−0.98 ± 0.18	−0.85 ± 0.30	1.34 ± 0.24	0.20 ± 0.09	82.33 ± 20.71	$1.22 \times 10^{11} \pm 1.80 \times 10^{10}$
vuds_cosmos_5180966608	1	4.53	0.76 ± 0.13	−0.80 ± 0.24	−0.68 ± 0.29	1.79 ± 0.26	0.33 ± 0.13	70.99 ± 17.94	$7.17 \times 10^{10} \pm 1.32 \times 10^{10}$
vuds_efdcs_530029038	1	4.43	0.00 ± 0.16	−1.92 ± 0.07	−0.64 ± 0.45	0.62 ± 0.17	0.14 ± 0.09	32.50 ± 6.47	$1.51 \times 10^{10} \pm 2.35 \times 10^9$
DEIMOS_COSMOS_434239	2	4.49	0.61 ± 0.08	−1.25 ± 0.26	−0.71 ± 0.33	1.49 ± 0.16	0.28 ± 0.12	103.13 ± 15.75	$2.74 \times 10^{10} \pm 7.85 \times 10^9$
DEIMOS_COSMOS_454608	2	4.58	0.33 ± 0.08	−1.45 ± 0.20	−1.23 ± 0.43	1.02 ± 0.13	0.11 ± 0.07	62.19 ± 8.09	$6.04 \times 10^9 \pm 1.55 \times 10^9$
DEIMOS_COSMOS_627939	2	4.53	0.48 ± 0.08	−1.46 ± 0.24	−0.75 ± 0.44	1.25 ± 0.13	0.24 ± 0.14	65.79 ± 5.93	$1.03 \times 10^{10} \pm 3.42 \times 10^9$
DEIMOS_COSMOS_630594	2	4.44	0.55 ± 0.09	−1.64 ± 0.25	−0.41 ± 0.36	1.37 ± 0.15	0.38 ± 0.17	57.27 ± 5.52	$6.28 \times 10^9 \pm 2.09 \times 10^9$
DEIMOS_COSMOS_845652	2	5.31	−0.20 ± 0.10	−1.73 ± 0.10	−1.84 ± 0.17	0.43 ± 0.09	0.02 ± 0.01	72.76 ± 7.19	$5.08 \times 10^{10} \pm 7.70 \times 10^9$
vuds_cosmos_5100541407	2	4.56	1.04 ± 0.09	−1.94 ± 0.26	0.23 ± 0.16	2.25 ± 0.19	1.25 ± 0.26	99.83 ± 11.58	$3.30 \times 10^{10} \pm 1.56 \times 10^{10}$
vuds_cosmos_5100559223	2	4.56	0.40 ± 0.18	−2.00 ± 0.22	−0.08 ± 0.45	1.11 ± 0.26	0.49 ± 0.27	34.92 ± 8.01	$9.51 \times 10^9 \pm 3.16 \times 10^9$
vuds_cosmos_510786441	2	4.46	−0.10 ± 0.10	−2.00 ± 0.10	−1.19 ± 0.45	0.48 ± 0.09	0.05 ± 0.04	61.60 ± 6.62	$1.18 \times 10^{10} \pm 2.18 \times 10^9$
vuds_cosmos_5110377875	2	4.55	0.65 ± 0.05	−1.38 ± 0.18	−0.55 ± 0.23	1.56 ± 0.09	0.34 ± 0.11	161.06 ± 9.09	$1.41 \times 10^{10} \pm 3.62 \times 10^9$